

Predicting the Pb-Bi-Po and Pb-Bi-Te phase diagrams from first principles

Michiel Gossye

Supervisor: Prof. dr. Stefaan Cottenier
Counsellors: Dr. ir. Kurt Lejaeghere, Jan Jaeken

Master's dissertation submitted in order to obtain the academic degree of
Master of Science in Engineering Physics

Department of Materials Science and Engineering
Chairman: Prof. dr. ir. Joris Degrieck
Faculty of Engineering and Architecture
Academic year 2014-2015





This work has been performed at the Center for Molecular Modeling.

Preface

About one year ago I was facing the important decision of how to complete my final year as an engineering student. Out of the numerous and diverse thesis topics, I chose a thesis at the Center for Molecular Modeling: the ab initio prediction of the ternary Pb-Bi-Po and Pb-Bi-Te phase diagrams. In the past year, I was given the opportunity to study this fascinating topic with the assistance of knowledgeable researchers in this study field.

The realization of this thesis is hence not only my merit, and I would like to thank the people that helped me in the past year. First of all, I want to thank my supervisor, prof. dr. Stefaan Cottenier. Thank you for your continuous help with my countless WIEN2k-problems and your insightful solutions when difficulties arose. I'd also like to thank my counsellors, dr. ir. Kurt Lejaeghere and Jan Jaeken, for giving meaningful advice and solutions whenever I needed them. Furthermore I want to thank ir. Michael Sluydts for helping me when I had IT-related problems.

The great atmosphere at the CMM was an indispensable aspect in the successful completion of my thesis. Therefore I would like to thank my colleague thesis students and friends Jelle, Sam, Bavo, Karel, Tom and Arthur for creating a motivating work environment.

Finally, I'd like to thank my parents for their incessant supportive attitude and for all the opportunities they have given me in the past years.

Michiel Gossye
May 22, 2015

Copyright agreement

The author gives permission to make this master's dissertation available for consultation and to copy parts of this master's dissertation for personal use.

In case of any other use, the limitations of the copyright have to be respected, in particular with regard to the obligation to state expressly the source when quoting results from this master's dissertation.

Michiel Gossye
May 22, 2015

Predicting the Pb-Bi-Po and Pb-Bi-Te phase diagrams from first principles

by

Michiel GOSSYE

Supervisor: prof. dr. Stefaan COTTENIER

Counsellors: Jan JAEKEN, dr. ir. Kurt LEJAEGHERE

Master's dissertation submitted in order to obtain the academic degree of
MASTER OF SCIENCE IN ENGINEERING PHYSICS

Department of Materials Science and Engineering

Chairman: prof. dr. ir. Joris DEGRIECK

Faculty of Engineering and Architecture

Academic year 2014-2015

Overview

This work addresses the prediction of the ternary Pb-Bi-Po and Pb-Bi-Te phase diagrams from first principles. Using density functional theory, the formation energies at 0 K of candidate crystals - selected based on chemical similarity to experimentally known crystals - are determined. A calculation scheme is worked out in order to predict the formation energy of each crystal to a sufficiently high precision. The predicted stable binary phases of the Pb-Bi-Po and Pb-Bi-Te systems match the experimental data. Four experimentally unknown stable binary crystals are predicted in the Bi-Po phase diagram. Furthermore, several ternary Pb-Bi-Po and Pb-Bi-Te phases are identified that have a fair chance to exist at room temperature as (meta)stable crystals. Thereafter, a correlation between the formation energies of Po- and corresponding Te-containing phases is determined.

Keywords

MYRRHA, DFT, Pb-Bi-Po, Pb-Bi-Te, ternary phase diagrams, database searching

Predicting the Pb-Bi-Po and Pb-Bi-Te phase diagrams from first principles

Michiel Gossye

Supervisor(s): prof. dr. Stefaan Cottenier

Counsellor(s): Jan Jaeken, dr. ir. Kurt Lejaeghere

Abstract—This work addresses the prediction of the ternary Pb-Bi-Po and Pb-Bi-Te phase diagrams from first principles. Using density functional theory, the formation energies at 0 K of candidate crystals - selected based on chemical similarity to experimentally known crystals - are determined. A calculation scheme is worked out in order to predict the formation energy of each crystal to a sufficiently high precision. The predicted stable binary phases of the Pb-Bi-Po and Pb-Bi-Te systems match the experimental data. Four experimentally unknown stable binary crystals are predicted in the Bi-Po phase diagram. Furthermore, several ternary Pb-Bi-Po and Pb-Bi-Te phases are identified that have a fair chance to exist at room temperature as (meta)stable crystals. Thereafter, a correlation between the formation energies of Po- and corresponding Te-containing phases is determined.

Keywords—MYRRHA, DFT, Pb-Bi-Po, Pb-Bi-Te, ternary phase diagrams, database searching

I. INTRODUCTION

COMPUTATIONAL physics may allow for advancement in materials research where experimental studies fall short. The assessment of the Pb-Bi-Po phase diagram is a case where a theoretical rather than an experimental treatment is particularly attractive, due to the presence of the radiotoxic Po. The Pb-Bi-Po phase diagram is of particular interest for the MYRRHA project at SCK•CEN [1]. With the MYRRHA project, the center has the goal to boost technological advancement in the development of generation IV nuclear fission reactors by supporting scientific research. Neutron capture of ^{209}Bi in the coolant of the reactor (lead-bismuth eutectic) leads to transmutation in ^{210}Po . The possible solidification of stable binary and ternary Pb-Bi-Po phases would decrease the amount of volatile Po that escapes the reactor, allowing a lower capacity of the Po-filters.

Because little is known about binary and ternary Po phases, the investigated crystals in this thesis are based on experimentally known crystals that show chemical similarity to the Pb-Bi-Po and Pb-Bi-Te systems. The Inorganic Crystallographic Structure Database (ICSD) is searched for all ternary crystals with elements belonging to group IV, V and VI and situated between the third and sixth period. The elements of these experimental crystals are then substituted by their chemical analogue in the sixth period. Although this method of database searching

M. Gossye is with the Center for Molecular Modeling, Ghent University (UGent), Ghent, Belgium. Email: Michiel.Gossye@UGent.be.

excludes any “new” crystal structures that are not observed in the chemically similar crystals, it leads to a smaller search space containing the most probable candidates.

The first-principles calculations on these hypothetical crystals determine the formation energy in the ground state. The predicted stability of the investigated crystals however is only valid in thermodynamical equilibrium. Nothing is known about energy barriers that need to be crossed to reach this most stable configuration, meaning that these barriers can allow metastable structures, which lie above the convex hull, to exist.

II. COMPUTATIONAL DETAILS

All calculations are performed within the DFT framework [2], using the PBE functional [3]. The Kohn-Sham equations are solved using the (Linearized) Augmented Plane Wave method with local orbitals ((L)APW+lo) [4], as implemented by WIEN2k [5]. The calculations include spin-orbit effects, which are not negligible for atoms belonging to the sixth period of the periodic system of elements. The used accuracy settings are (a) number of k-points= $184.000/\text{\AA}^{-3}$, (b) $\text{rk}_{\text{max}}=8$ and (c) $\Delta E=E_{\text{F}}+7$ Ry, leading to an estimated calculation precision of ± 5 meV/atom.

Substituting the atoms of the experimental crystals in the search space by Pb, Bi and Po/Te will lead to a change in equilibrium volume. This new minimum is determined by fitting a third-order Birch-Murnaghan equation of state [6].

$$E(V) = E_0 + \frac{9V_0B_0}{16} \left\{ \left[\left(\frac{V_0}{V} \right)^{2/3} - 1 \right]^3 + \left[\left(\frac{V_0}{V} \right)^{2/3} - 1 \right]^2 \left[6 - 4 \left(\frac{V_0}{V} \right)^{2/3} \right] \right\} \quad (1)$$

Afterwards, the atomic positions are relaxed to the configuration with the lowest formation energy. It is found that these two steps are sufficient to determine the formation energy. As a test, the lattice parameter ratio was also optimized using a quadratic interpolation of the calculated data points (in order to approximate the optimal unit cell even better) for a representative subset of the search space. The lowering in formation energy turns

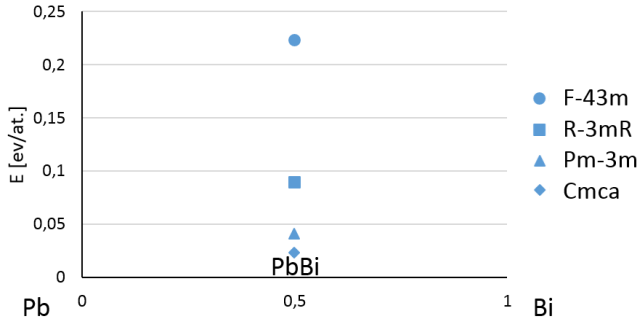


Fig. 1: The binary phase diagram of Pb-Bi, calculated from first principles.

out to be smaller than the calculation precision and is hence not taken into account in the other calculations.

III. BINARY PHASE DIAGRAMS CONTAINING PB, BI, PO OR TE

For the binary Pb-Te, Pb-Bi and Bi-Te phase diagrams, experimental data are available [7]. On the other hand, there is nothing known about the Pb-Po and Bi-Po phase diagrams apart from the experimentally observed PbPo [8]. ICSD is therefore searched for binary crystals with elements in the fifth and sixth period that are chemically similar to the earlier mentioned phases. DFT predictions are made for all five phase diagrams.

The Pb-Bi phase diagram predicted from first principles is shown in figure 1. No experimental stable Pb-Bi phases are known, in agreement with the DFT prediction: all four crystals have a positive formation energy.

Four crystals belonging to the Pb-Po and Pb-Te phase diagrams are investigated. The DFT predicted phase diagrams are visualised in figure 2. Two experimental Pb-Te phases are known, corresponding to the two most stable crystals in the Pb-Te phase diagram. The predicted stable PbPo phase also matches experimental observations [8]. Comparing the Pb-Te phase diagram with the Pb-Po phase diagram, one can observe a systematically weaker binding in the latter.

Eight crystals are investigated for the prediction of the Bi-Po and Bi-Te phase diagrams. The results are visualized in figure 3. The correspondence between the stability of matching Po- and Te-crystals is again clearly present. Four stoichiometries ($\text{Bi}_2\text{Po}/\text{Bi}_2\text{Te}$, $\text{Bi}_4\text{Po}_3/\text{Bi}_4\text{Te}_3$, BiPo/BiTe and $\text{Bi}_2\text{Po}_3/\text{Bi}_2\text{Te}_3$) are predicted to be stable. These crystal structures of the Bi-Te phase diagram are also experimentally known. The similarity between the predicted Pb-Bi, Pb-Te and Bi-Te phase diagrams with experimental results validates the DFT results. The predicted Pb-Po and Bi-Po phase diagrams and in extension the

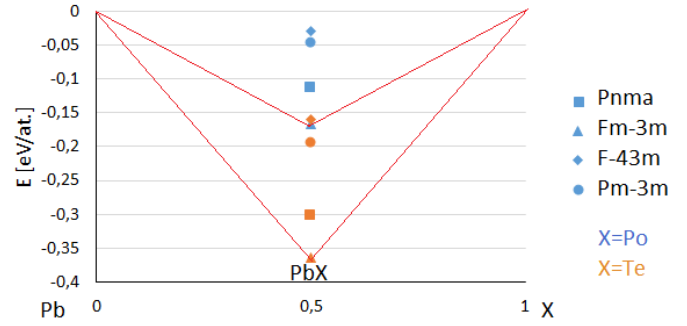


Fig. 2: The binary phase diagram of Pb-Po (blue data points) and Pb-Te (orange data points), calculated from first principles. The convex hulls of the Pb-Po and Pb-Te diagrams are indicated in red.

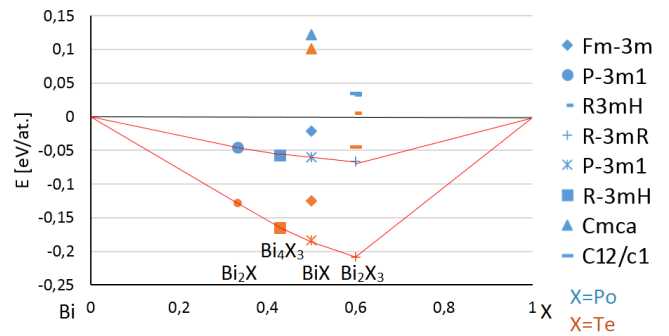


Fig. 3: The binary phase diagram of Bi-Po (blue datapoints) and Bi-Te (orange data points), calculated from first principles. The convex hulls of the Bi-Po and Bi-Te diagrams are indicated in red.

ternary Pb-Bi-Te and Pb-Bi-Po phase diagrams, for which experimental verification is limited, can hence be considered reliable. This means that four experimentally unknown stable Bi-Po phases are predicted.

Rijpstra et al. studied the correlation between the solution enthalpy of Po and Te in Ref. [9]. Their three data points are added to the data of the binary crystals calculated in this work (after a recalculation due to a different definition: in this study the formation energy is plotted). This is shown in figure 4. A linear correlation is present, making it possible to write the formation energy after a least-squares fit as:

$$\Delta E_{Po}[eV/at.] = 0,572 \cdot \Delta E_{Te}[eV/at.] + 0,050eV/at. \quad (2)$$

IV. TERNARY PB-BI-PO AND PB-BI-TE PHASE DIAGRAMS.

Nineteen crystals belonging to the Pb-Bi-Po and Pb-Bi-Te phase diagrams are investigated. Most crystals can be decomposed in a combination of the stable $\text{Bi}_2\text{Po}_3/\text{Bi}_2\text{Te}_3$ and

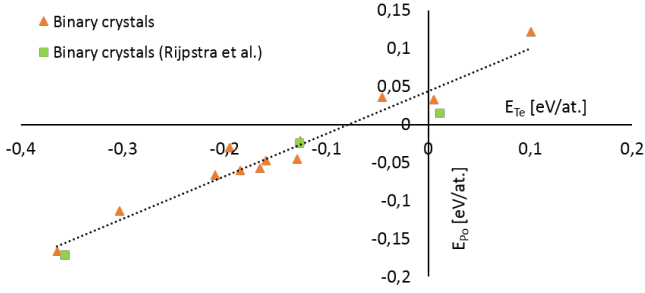


Fig. 4: Correlation of the formation energies of Po and Te in binary crystals. Data points by Rijpstra et al. [9] are added to the data set of this work.

PbPo/PbTe phases. The larger stability of Bi_2Te_3 and PbTe compared to Bi_2Po_3 and PbPo respectively leads to a comparable stability for analogous ternary Po and Te crystals, even though the formation energy of the Te-crystals when compared to elemental solids is systematically lower than the formation energy of the corresponding Po crystals.

Negative formation energies are found for the PbBi_4Po_7 and PbBi_2Te_4 stoichiometries, but the formation energy values are an order of magnitude smaller than the calculation precision, meaning one has to be careful when interpreting these results. Statements about the stability of these crystals can therefore not be made with certainty. $\text{Pb}_2\text{Bi}_2\text{Te}_5$, predicted to be unstable by both WIEN2k and VASP [10], is mentioned as a topological insulator in Ref. [11]. The study however is strictly theoretical, experimental observations of $\text{Pb}_2\text{Bi}_2\text{Te}_5$ are not mentioned. This crystal, lying 0,017 eV/atom (WIEN2k) above the convex hull could be metastable, since some metastable crystals have been found to possess formation energies of up to 0,1 eV/atom, e.g. ZnO_2 [12]. This possible metastability is applicable to a large subset of the inspected ternary crystals.

Materials Project [10] contains three ternary (metastable) crystals belonging to Pb-Bi-Te phase diagram. In addition, there are five binary crystals investigated in this thesis that are also calculated in Materials Project. All formation energies of crystals of Materials Project are calculated using VASP. The comparison of the WIEN2k- and VASP-results is made in table I.

For all but one crystal (BiTe ($\text{Fm}\bar{3}\text{m}$)) VASP shows a small overestimation of the formation energy. The correspondence between both DFT codes is therefore quite good.

The formation energies of the ternary crystals can be added to the correlation plot in figure 4. Formation energies of the ternary crystals should be expressed as a function of the elementary solids (instead of the most stable decomposition of binary crystals) in order to be comparable to the data points of the bi-

Formula	Space Group	WIEN2k (EL.) [eV/at.]	VASP (EL.) [eV/at.]	ΔE [eV/at.]
Bi_4Te_3	$\text{R}\bar{3}\text{m}$	-0,165	-0,173	0,008
BiTe	$\text{P}\bar{3}\text{m1}$	-0,184	-0,199	0,015
BiTe	$\text{Fm}\bar{3}\text{m}$	-0,126	-0,069	-0,057
Bi_2Te_3	$\text{R}\bar{3}\text{m}$	-0,209	-0,237	0,028
PbTe	$\text{Fm}\bar{3}\text{m}$	-0,364	-0,414	0,050
PbBi_4Te_7	$\text{P}\bar{3}\text{m1}$	-0,232	-0,266	0,034
PbBi_2Te_4	$\text{R}\bar{3}\text{mH}$	-0,250	-0,286	0,036
$\text{Pb}_2\text{Bi}_2\text{Te}_5$	$\text{P}\bar{3}\text{m1}$	-0,226	-0,258	0,032

TABLE I: Comparison of the calculations made by WIEN2K and VASP for binary and ternary crystals. Columns from left to right: (1) Chemical formula, (2) Space group, (3) and (4) Formation energy when compared to decomposition in elementary solids (also for ternary crystals) for WIEN2k and VASP [10], (5) Difference in formation energy between the WIEN2k-results and VASP-results [10].

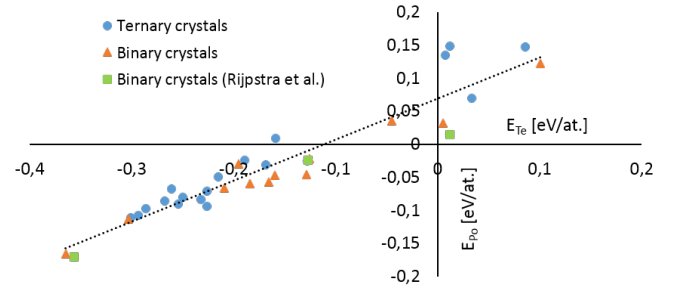


Fig. 5: Correlation of the formation energies of the binary and ternary Po- and Te-containing crystals (based on the formation energies with respect to decomposition in elementary solids). Data points by Rijpstra et al. are added [9].

nary crystals. The new data is visualised in figure 5.

The correlation of the formation energies, after a least-squares fit, is given by following formula, which is similar to the earlier found relation in 2, as expected.

$$\Delta E_{Po}[\text{eV/at.}] = 0,621 \cdot \Delta E_{Te}[\text{eV/at.}] + 0,069\text{eV/at.} \quad (3)$$

The real formation energies (no longer with respect to the solid elements) of the ternary crystals containing Po and Te can also be compared. Once again, a linear correlation is found, corresponding to the relation:

$$\Delta E_{Po}[\text{eV/at.}] = 0,770 \cdot \Delta E_{Te}[\text{eV/at.}] + 0,009\text{eV/at.} \quad (4)$$

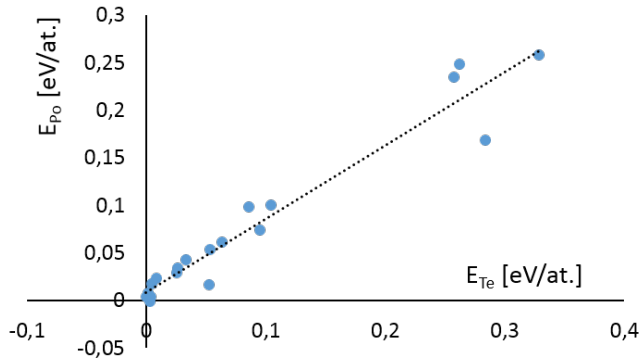


Fig. 6: Correlation of the formation energies of the ternary Po- and Te-containing crystals, based on the formation energies.

The results are shown in figure 6. The correlation between crystals containing Po and Te in figure 5 and 6 is due to chemical similarity between Po and Te atoms. Relations 3 and 4 make it possible to predict the stability of Po crystals by investigating the matching Te crystals.

V. CONCLUSION

In this thesis the ternary Pb-Bi-Po and Pb-Bi-Te phase diagrams and corresponding binary phase diagrams are predicted using DFT. First, the five binary phase diagrams are determined from first principles. Experimental data are available for three phase diagrams. The correspondence with the DFT results validates the reliability of the predicted phase diagrams, binary and ternary, for which experimental data are lacking. In this way, four stable and experimentally unknown binary Bi-Po phases are predicted. Next, the ternary Pb-Bi-Po and Pb-Bi-Te phase diagrams are predicted and they show a negative formation energy for PbBi_4Po_7 and PbBi_2Te_4 . Caution has to be taken into account when interpreting these values, being an order of magnitude smaller than the calculation precision. However, it is very likely that stable Pb-Bi-Po and Pb-Bi-Te phases may be found when the present work is extended with an unbiased structure prediction method (e.g. a genetic algorithm), applied to the stoichiometries with almost zero formation energy (e.g. 1:2:4 and 1:4:7). Temperature dependent predictions for the free energy can also be attempted. In both cases, this would require an order of magnitude more computation time. Finally, a relation between the formation energies of Po and Te is determined, suggesting that experiments using Te can be used to predict the behaviour of Po, reducing the number of required experiments with this element.

VI. ACKNOWLEDGEMENTS

This thesis was performed at the Center for Molecular Modeling (CMM), under supervision of prof. dr. Stefaan Cottenier, dr. ir. Kurt Lejaeghere and Jan Jaeken. I wish to thank them for their support and guidance throughout the realization of this work. The computational resources and services used were provided by Ghent University (Stevin Supercomputer Infrastructure).

REFERENCES

- [1] <http://myrrha.sckcen.be>
- [2] P. Hohenberg and W. Kohn. Inhomogeneous Electron Gas. *Phys. Rev.* 136:B864-B871. 1964.
- [3] J. P. Perdew, K. Burke and M. Ernzerhof. Generalized gradient approximation made simple. *Phys. Rev. Lett.*, 77:3865-3868. 1996.
- [4] E. Sjöstedt, L. Nordström and D. J. Sing. An alternative way of linearizing the augmented plane-wave method. *Solid State Commun.*, 114(1):15-20. 2000.
- [5] P. Blaha, K. Schwarz, P. Sorantin and S. B. Trickey. Full-potential, linearized augmented plane wave programs for crystalline systems. *Computer Physics Communications*, 59(2):399-415. 1990.
- [6] Birch, F. Finite elastic strain of cubic crystals. *Phys. Rev.*, 71:809824. 1947.
- [7] Alloy Phase Diagrams Volume 3. *ASM International*. 1992.
- [8] H. Feuerstein, J. Oschinski and S. Horn. Behavior of Po-210 in Molten Pb-17Li. *Journal of Nuclear Materials*, 191-194, Part A(0):288-291. 1992.
- [9] K. Rijpstra, A. Van Yperen-De Deyne, J. Neuhausen, V. Van Speybroeck and S. Cottenier. Solution enthalpy of Po and Te in solid leadbismuth eutectic. *Journal of Nuclear Materials*, 450(1-3):287291. 2014.
- [10] <https://www.materialsproject.org>
- [11] I. V. Silkin, Yu. M. Koroteev, S. V. Eremeev, G. Bihlmayer and E. V. Chulkov, Three and Two-dimensional Topological Insulators in $\text{Pb}_2\text{Sb}_2\text{Te}_5$, $\text{Pb}_2\text{Bi}_2\text{Te}_5$, and $\text{Pb}_2\text{Bi}_2\text{Se}_5$ Layered Compounds. *JETP Letters*, 94(3):217-221. 2011.
- [12] K. Rijpstra. Density functional theory as a tool to get more out of experimental data: case-studies for Al-Zn-O and for the interaction between Po and Pb-Bi-eutectic. 2014.

Contents

Preface	i
Copyright agreement	iii
Overview	iii
Extended abstract	iv
Contents	viii
List of Figures	x
List of Tables	xii
Abbreviations	xiii
1 Introduction and objective	1
1.1 Phase diagrams	2
1.1.1 Introduction	2
1.1.2 Method overview	3
1.1.2.1 Cluster expansion	5
1.1.2.2 Database searching	6
1.1.2.3 Unbiased structure prediction	7
1.2 Relevance of the Pb-Bi-Po phase diagram for MYRRHA	8
1.2.1 Introduction to MYRRHA	8
1.2.2 Nuclear reactors	9
1.2.3 MYRRHA: a generation IV reactor	10
1.2.4 Po-contamination of LBE	10
1.3 Analogy between Pb-Bi-Po and Pb-Bi-Te phases	11
2 Density Functional Theory	13
2.1 The many-body problem	13
2.2 The Born-Oppenheimer approximation	14
2.3 Density functional theory	14
2.4 Spin-orbit coupling	15
2.5 WIEN2k parameters	18
2.5.1 Number of k-points	18
2.5.2 $r_{k_{max}}$	19
2.5.3 E_{max}	19

3	Methodology	20
3.1	Convergence tests	20
3.1.1	Number of k-points convergence test	20
3.1.2	rk_{max} convergence test	21
3.1.3	E_{max} convergence test	22
3.2	Calculation scheme	23
3.2.1	Volume optimization	23
3.2.2	Geometry optimization	24
3.2.3	Ratio optimization	24
4	Binary Phase Diagrams Containing Pb, Bi, Po or Te	27
4.1	Introduction	27
4.2	The Pb-Bi phase diagram	27
4.3	The Pb-Te and Pb-Po phase diagram	28
4.4	The Bi-Te and Bi-Po phase diagram	31
4.5	Correlation between binary phases containing Po and Te	33
5	Ternary Pb-Bi-Te and Pb-Bi-Po Phase Diagrams	36
5.1	Introduction	36
5.2	Stability of the ternary crystals	37
5.3	Correlation between ternary phases containing Po and Te	40
6	Conclusion and Outlook	44
A	Binary Phase Results	46
B	Ternary Phase Results	47
	Bibliography	48

List of Figures

1.1	Left: Phase diagram visualizing the ternary phases containing an 80% concentration of A (blue) and an A:C-ratio of 2:3 (red). Right: Indication of the phase $A_2B_2C_5$	3
1.2	An energy barrier can prevent structures from transforming from A to the more stable structure B, resulting in a metastable phase A.	3
1.3	Formation enthalpy of all structures calculated within the Al-Zn-O system. Formation energy is in eV/atom. The formation energy scale on the ternary phase graph is ten times smaller than on the two binary phase graphs on the side [2].	4
1.4	The ternary Pb-Bi-Te phase diagram from Materials Project. No stable ternary phases are yet known.	5
1.5	The input structure in the cluster expansion method is the rocksalt structure [3].	6
1.6	Group IV, V and VI of the PSE. Original crystal elements should be replaced by Pb, Bi and Po/Te.	7
1.7	Visualisation of MYRRHA at SCK•CEN [12].	9
1.8	Correlation between the solution enthalpies of Po and Te in LBE (1/16), elemental Pb (various concentrations), and in elemental Bi (1/24). Additionally, the same correlation for full substitution of either Pb or Bi by Po or Te is given for PbBi (NaCl-structure) and for Bi_4Pb_3 . Every data point corresponds to a different local environment for Po/Te. In the two calculations that lead to every data point, all atomic positions were independently optimized (= the distance between Te and its neighbours is allowed to be different from the distance between Po and its neighbours). The dashed line is a similar fit through three well-separated data points, now taking spin-orbit coupling into account (from left to right: Bi-substitution in PbBi [NaCl], Pb-substitution in PbBi [NaCl]; 25% of Po/Te in fcc-Pb) [18].	12
2.1	Scheme of the different crystal regions. Core electrons and valence electrons form the atomic sphere region or MTS region. All other space is interstitial space between the atoms [37].	18
3.1	Graph of the convergence of number of $k - points$. The x-axis is the normalized number of $k - points$ according to equation 3.1. The y-axis is the energy error per atom.	21
3.2	Graph of the convergence of $r^{k_{max}}$ -value. The x-axis shows the $r^{k_{max}}$ -value. The y-axis is the energy error per atom.	22
3.3	Graph of the convergence of E_{max} -value. The x-axis shows the E_{max} -value. The y-axis is the energy error per atom.	23
3.4	Third order Birch-Murnaghan fit.	24
3.5	Schematical representation of the working principle of double loop optimization (left) versus MSR1a (right).	25

3.6	Graphical representation of the ratio optimization procedure for PbBi_2Po_4 . On the left: schematical representation of each of the 27 possible configurations. On the right: 3 plots corresponding to the c-parameter changed by -2% , 0% and 2% . The difference in total energy before and after ratio optimization is given. In the red region for $a=0$, $b<0$, $c=0$, the energy lowers, resulting in a more stable configuration.	26
4.1	The Pb-Bi phase diagram, calculated from first principles.	28
4.2	The experimental Pb-Bi phase diagram [45]. No experimentally stable phases in the ground state are known.	29
4.3	The Pb-Te and Pb-Po phase diagram, calculated from first principles.	30
4.4	Experimental Pb-Te phase diagram. The PbTe phase in the $\text{Fm}\bar{3}\text{m}$ and Pnma crystals structure are stable in the ground state [45].	30
4.5	The Bi-Te and Bi-Po phase diagram, calculated from first principles.	31
4.6	Experimental Bi-Te phase diagram [45].	32
4.7	The binary Bi-Te phase diagram calculated by VASP, from Materials Project.	33
4.8	Correlation between the formation energy of Po and Te for the binary phases. The blue data points correspond to the binary phases calculated in this thesis. The orange data points correspond to the binary phases calculated by Rijpstra et al. in Ref. [18].	35
4.9	Comparison between the DFT results for the Pb-Po phase diagram and the results obtained using the correlation with the Pb-Te phase diagram.	35
4.10	Comparison between the DFT results for the Bi-Po phase diagram and the results obtained using the correlation with the Bi-Te phase diagram.	35
5.1	Set of ternary crystals origination from the third to the sixth period of the PSE. Blue data points are calculated. Red data points could not be calculated due to computational limitations (see text).	38
5.2	Decomposition of the ternary crystals into stable binary phases. Blue data points correspond to $\text{X}=\text{Po}$. Orange data points correspond to $\text{X}=\text{Te}$	39
5.3	Formation energy of the crystals that are composed of Bi_2Po_3 and PbPo. Corresponding crystal structures for Po- and Te-crystals are represented by the same symbol. From left to right (and from less to more stable for the Te-crystals in case of multiple structures): $\text{PbBi}_6\text{X}_{10}$, PbBi_4X_7 , $\text{Pb}_3\text{Bi}_8\text{X}_{15}$, PbBi_2X_4 (Pnma), PbBi_2X_4 ($\text{R}\bar{3}\text{mH}$), PbBi_2X_4 ($\text{P}\bar{3}\text{m1}$), $\text{Pb}_2\text{Bi}_2\text{X}_5$ (Pnma), $\text{Pb}_2\text{Bi}_2\text{X}_5$ ($\text{P}\bar{3}\text{m1}$), $\text{Pb}_2\text{Bi}_2\text{X}_5$ (Pbnm), $\text{Pb}_3\text{Bi}_2\text{X}_6$ (C2/m), $\text{Pb}_3\text{Bi}_2\text{X}_6$ ($\text{R}\bar{3}\text{mH}$) $\text{Pb}_4\text{Bi}_2\text{X}_7$ and $\text{Pb}_2\text{Bi}_6\text{X}_9$	40
5.4	Correlation between the formation energy of Po and Te for the binary and ternary phases w.r.t. the elementary soldis.	42
5.5	Correlation between the formation energy of Po and Te for the ternary phases w.r.t. the most stable decomposition.	42
5.6	Comparison between the DFT formation energies and the formation energies obtained using the correlation with the Pb-Bi-Te phase diagram for the Bi_2Po_3 - PbPo cross section of the ternary Pb-Bi-Po phase diagram. Corresponding crystal structures for Po- and Te-crystals are represented by the same symbol. From left to right (and from less to more stable for the Te-crystals in case of multiple structures): $\text{PbBi}_6\text{X}_{10}$, PbBi_4X_7 , $\text{Pb}_3\text{Bi}_8\text{X}_{15}$, PbBi_2X_4 (Pnma), PbBi_2X_4 ($\text{R}\bar{3}\text{mH}$), PbBi_2X_4 ($\text{P}\bar{3}\text{m1}$), $\text{Pb}_2\text{Bi}_2\text{X}_5$ (Pnma), $\text{Pb}_2\text{Bi}_2\text{X}_5$ ($\text{P}\bar{3}\text{m1}$), $\text{Pb}_2\text{Bi}_2\text{X}_5$ (Pbnm), $\text{Pb}_3\text{Bi}_2\text{X}_6$ (C2/m), $\text{Pb}_3\text{Bi}_2\text{X}_6$ ($\text{R}\bar{3}\text{mH}$) $\text{Pb}_4\text{Bi}_2\text{X}_7$ and $\text{Pb}_2\text{Bi}_6\text{X}_9$	43

List of Tables

4.1	From left to right: (1) Original experimental crystals, (2) corresponding space group, (3) index number of the CIF-file in ICSD, (4) crystal with substituted Pb- and Bi-atoms.	28
4.2	From left to right: (1) Original experimental crystals, (2) corresponding space group, (3) index number of the CIF-file in ICSD, (4) crystal with substituted Pb- and Po/Te atoms.	29
4.3	From left to right: (1) Original experimental crystals, (2) corresponding space group, (3) index number of the CIF-file in ICSD, (4) crystal with substituted Bi- and Po/Te atoms.	31
4.4	Comparison of the data points of the Bi-Te and Pb-Te phase diagram, calculated by WIEN2K and VASP. From left to right: (1) Chemical formula, (2) corresponding space group, (3) formation energy calculated by WIEN2k, (4) formation energy calculated by VASP, (5) difference in formation energy between the WIEN2k and VASP calculations.	33
5.1	From left to right: (1) Original experimental crystals, (2) corresponding space group, (3) index number of the CIF-file in ICSD, (4) crystal with substituted Bi- and Po/Te-atoms.	37
5.2	Comparison of data points of the Pb-Bi-Te phase diagram, calculated by WIEN2K and VASP. Columns from left to right: (1) Chemical formula of the crystal, (2) corresponding space group, the formation energy energy in comparison with the elementary solids, calculated with WIEN2k (3) and VASP (4), (5) the energy difference between the WIEN2k- and the VASP-result, the formation energy (in comparison with the decomposition in stable binary crystals) calculated by WIEN2k (6) and VASP (7) and (8) the energy difference between the WIEN2k- and the VASP-result.	40
A.1	Columns from left to right: (1) all investigated binary phases of the Pb-Bi-Po and Pb-Bi-Te systems, (2) corresponding space group,(3) index of the CIF in ICSD, (4) formation energy in ev/atom.	46
B.1	Columns from left to right: (1) all investigated ternary crystals (with X=Po or Te), (2) the corresponding space group, (3) the formation energy w.r.t. the elementary solids of the Po-crystals (3) and the Te-crystals (4), the formation energy w.r.t. decomposition in stable binary and/or elementary crystals of the Po-crystals (5) and of the Te-crystals (6).	47

Abbreviations

ECI	E ffective C luster I nteraction
ATAT	A lloy T heoretic A utomatic T oolkit
EAM	E mbdedd A tom M odel
AIRSS	A b I nitio R andom S tructure S earching
PSE	P eriodic S ystem of E lements
SEM	S canning E lectron M icroscope
DFT	D ensity F unctional T heory
PES	P otential E nergy S urface
MYRRHA	M ulti-purpose H ybrid R esearch R eactor for H igh-tech A pplications
ADS	A ccelerator D riven S ystem
LBE	L ead- B ismuth E utectic
KS	K ohn- S ham
HOMO	H ighest O ccupied M olecular O rbital
PBE	P erdew- B urke- E rnzerhof
GGA	G eneralized G radient A pproximation
LDA	L ocal- D ensity A pproximation
LAPW+lo	L inearized A ugmented P lane W ave + l ocal o rbitals
APW	A ugmented P lane W ave
LAPW	L inearized A ugmented P lane W ave
MTS	M uffin T in S phere
E_F	F ermi E nergy
EOS	E quation O f S tate
ICSD	I norganic C rystal S tructure D atabase
SCF	S elf C onsistent F ield
CIF	C rystallographic I nformation F ile
RMS	R oot M ean S quare

Chapter 1

Introduction and objective

“One of the continuing scandals in the physical sciences is that it remains in general impossible to predict the structure of even the simplest crystalline solids from knowledge of their chemical composition.”

— John Maddox

Any scientific field that gained some maturity can be approached in three different but intertwined ways. A first is the experimental approach, where one observes the way nature behaves under different circumstances and initial conditions. Discovering patterns in nature’s behaviour leads to an underlying theoretical model, which is a second way of looking at science. The third one is simulation, where formulas deduced from theory are applied to predict what will happen in practice.

Nowadays it is straightforward to calculate the final speed and falling time of the apple that landed on Newton’s head almost 400 years ago. This is done by simulating; the theoretical equations behind classical mechanics are known and can be solved. When looking at quantum mechanics, the story is a little different. Even though the equation that describes quantum systems - the Schrödinger equation - is known, it is not possible to solve a quantum many-body system exactly. Approximations have to be made that will lead to reliable results in a lot of cases.

With the continuously increasing computer processor speed that is achieved by contemporary technological progress in this field, computational physics is an exciting and promising way to predict characteristics of materials. It is possible to examine properties of a very large set of materials, which would be too time-demanding to do experimentally. Or, as is the case in this thesis, the properties of a phase diagram containing a radiotoxic element - polonium - can be predicted in a safe, virtual environment.

1.1 Phase diagrams

1.1.1 Introduction

The objective of this thesis is to determine the phase diagrams of Pb-Bi-Po and Pb-Bi-Te in the ground state (at 0 K). Such a ternary phase diagram can be graphically represented in two-dimensional space by a triangle. The phase has only two linearly independent variables since the concentrations of the three elements has to sum to 100%. A schematical representation of a ternary phase diagram is given in figure 1.1. In the corners of the diagrams one finds the three elements (A, B and C). The concentration of a specific element decreases linearly with increasing distance from their respective corner. On the edges of the triangle, the binary A-B, A-C and B-C phases are found. A binary crystal A_nB_m is situated on the A-B edge, and lies closer to the A-point as n is larger than m. The ternary phases lie in the bulk of the triangle. The concentration of each element can be read from the figure, but the method is less trivial for ternary phases. One method is to determine the shortest distances from the bulk point to the three edges of the diagram. When one normalises these distances with respect to the height of the triangle, one gets the concentration of each element in the phase.

An illustration of this is given in the two diagrams of figure 1.1. The blue line in the left phase diagram indicates all phases containing 80% of element A. This includes the binary phases A_4B and A_4C at the edges, as well as an infinite number of ternary phases (e.g. A_8BC) on the straight line segment inside the triangle. When one determines the distance of a point of this horizontal to the B-C-line, one finds indeed a distance that is equal to 80% of the total height of the triangle. The red line in the left phase diagram indicates all phases where the ratio of the elements A:C equals 2:3. When one determines the distances of each point of this line to the sides B-C and A-B, one finds that the latter distance is 1,5 times the first distance. As a last illustration, the crystal $A_2B_2C_5$ is marked in the right phase diagram of figure 1.1. The distances to the sides of the diagram are indicated, and sum to the total height of the phase diagram. One finds a ratio of 2:2:5 for this crystal.

A realistic example of a ternary phase diagram, containing elements Zn, Al and O, can be found in figure 1.3. For the Zn-O, Al-O and ZnO- Al_2O_3 -lines, diagrams are added which show the formation energy starting from the two end members (i.e. Zn and O, ZnO and Al_2O_3 , etc.). A convex hull can be drawn: the collection of straight line segments that continuously connects the left and the right point such that no other point lies below the line segments. Compositions on the convex hull are stable. Solids above the convex hull are not thermodynamically stable: their energy can be lowered by decomposing them into a combination of the two nearest stable phases. Metastability occurs when an energy barrier has to be crossed in order to reach a more stable configuration: these structures can still exist without spontaneous decomposition or change of crystal structure. This concept is schematically illustrated in figure 1.2. The ternary phase diagram only gives information on the crystals in thermodynamic equilibrium, there is nothing

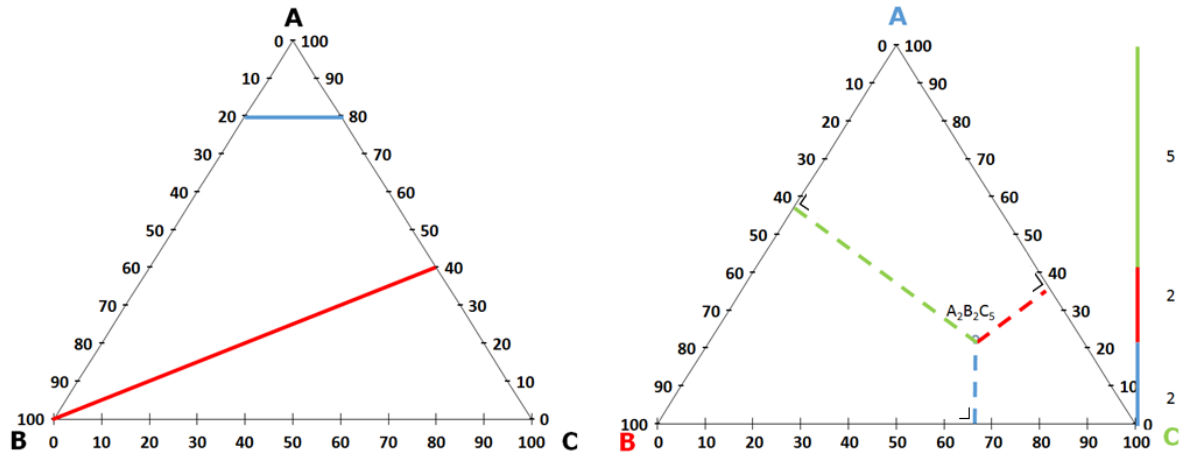


FIGURE 1.1: Left: Phase diagram visualizing the ternary phases containing an 80% concentration of A (blue) and an A:C-ratio of 2:3 (red). Right: Indication of the phase $A_2B_2C_5$.

known about the possible energy barriers preventing to reach these most stable structures.

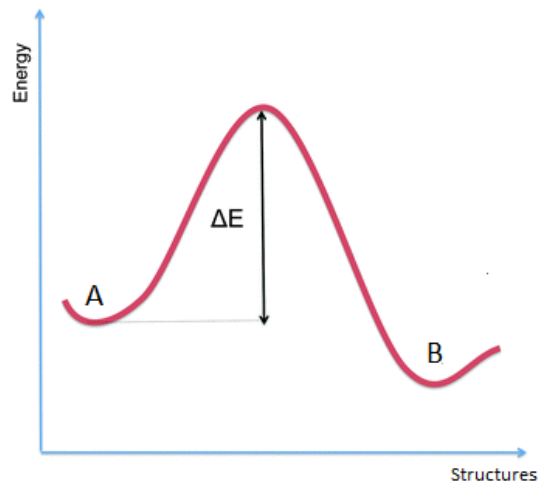


FIGURE 1.2: An energy barrier can prevent structures from transforming from A to the more stable structure B, resulting in a metastable phase A.

1.1.2 Method overview

Almost nothing is known about stable binary or ternary crystal structures of the Pb-Bi-Po phase diagram yet. A couple of ternary phases of the Pb-Bi-Te phase diagram are known. Figure 1.4 from Materials Project [1] shows the latter diagram, determined from first principles. Only binary phases (Bi_2Te_3 , Bi_4Te_3 , Bi_8Te_9 and $PbTe$) are found to be stable. Three ternary phases ($PbBi_4Te_7$, $Pb_2Bi_2Te_5$ and $PbBi_2Te_4$) are calculated in Materials Project but have a formation energy lying above the convex hull. They are not included in the phase diagram because they

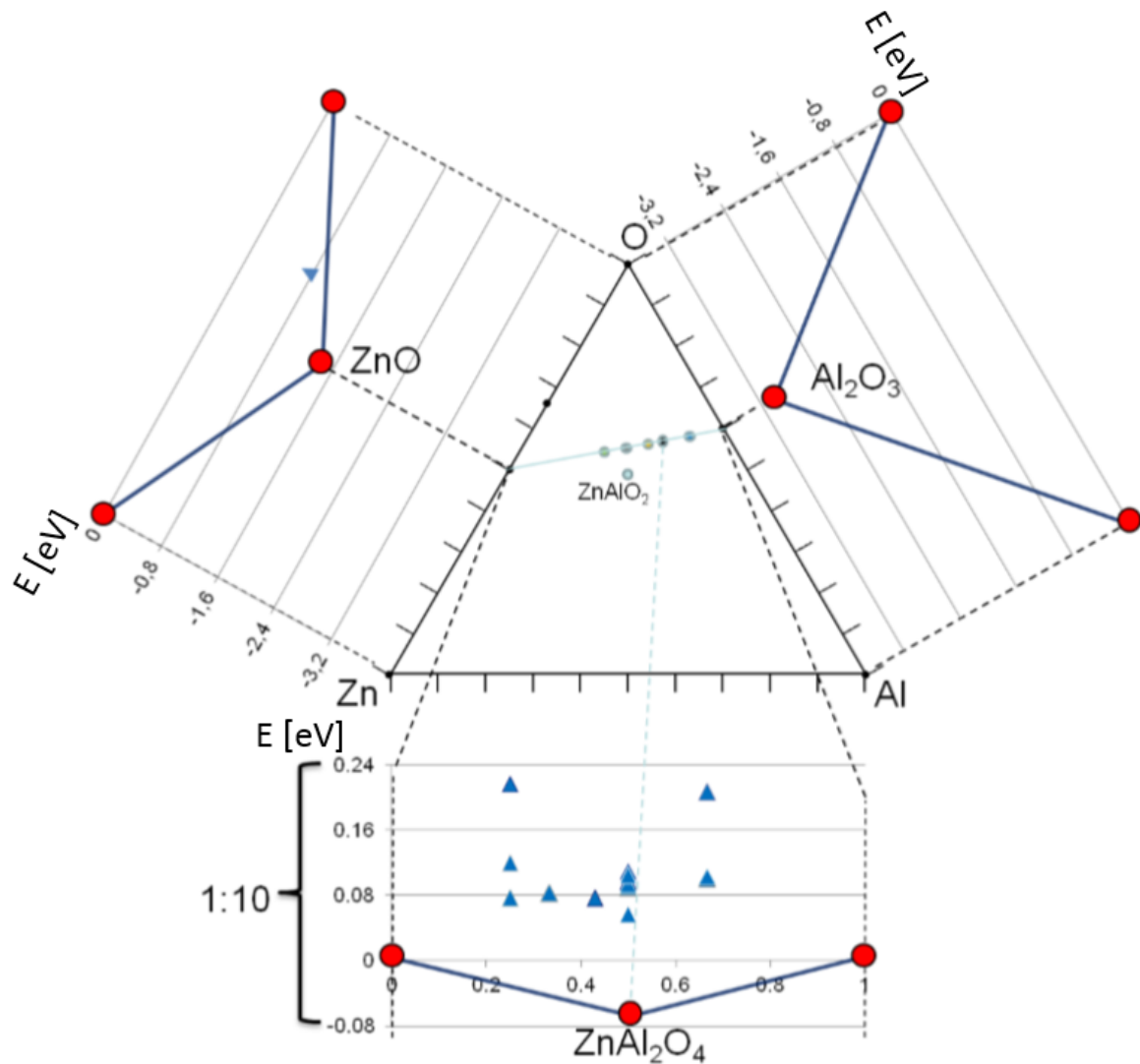


FIGURE 1.3: Formation enthalpy of all structures calculated within the Al-Zn-O system. Formation energy is in eV/atom. The formation energy scale on the ternary phase graph is ten times smaller than on the two binary phase graphs on the side [2].

are metastable.

The crystals in the phase diagram in figure 1.4 are experimentally known and the formation energy is afterwards calculated using first principles. The determination of stable configurations is not trivial without this experimental knowledge. One cannot easily deduce the stable crystal structure when the chemical composition of a crystal is given. One of the difficulties lies in the fact that crystal structures that differ a lot can have similar formation enthalpies. In this section three main methods are evaluated that could be applicable to determine the Pb-Bi-Po and Pb-Bi-Te phase diagrams from first principles. These methods differ with respect to the size of the set of searched crystal structures. The first method uses the cluster expansion formalism to search the set of all configurations of one imposed crystal structure. The second method allows more freedom in the searched set by looking at possible structures that are found due to

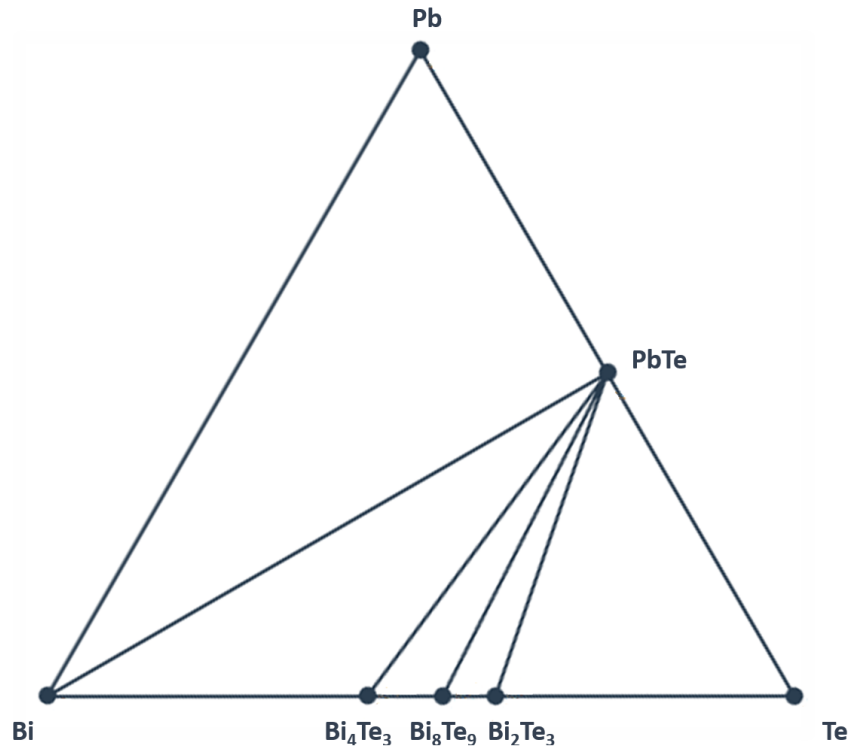


FIGURE 1.4: The ternary Pb-Bi-Te phase diagram from Materials Project. No stable ternary phases are yet known.

chemical similarity with experimentally known crystals. The last method, unbiased structure prediction, is the most general of the three methods: the entire potential energy surface (PES) is searched for minima.

1.1.2.1 Cluster expansion

In Ref. [3], Wolverton et al. used cluster expansion to determine the phase diagram of Sr-Pb-S and Ca-Pb-S. In the cluster expansion formalism, the possible crystal structures should be given as input. SrPb, PbS and CaPb, the parent crystals of both ternary structures, have the rocksalt structure. This structure is then the predetermined structure of the daughter crystal (see figure 1.5).

It is not possible to calculate all possible atomic configurations using DFT. Cluster expansion is a method that will use a limited number of input structures to predict the energy of other crystal structures. It is a way of coarse-graining the atomic configuration space. In this formalism, the configurational dependence of the alloy's energy is represented as a polynomial function [4]. The variables in this expansion are pseudospin variables and their value determines the configuration for a specific lattice site. The phase diagrams studied by Wolverton et al. are ternary, meaning that the pseudospin variable σ_i takes on three values (-1, 0 and 1) depending on the atom on lattice position i [5]. The energy can then be written as follows:

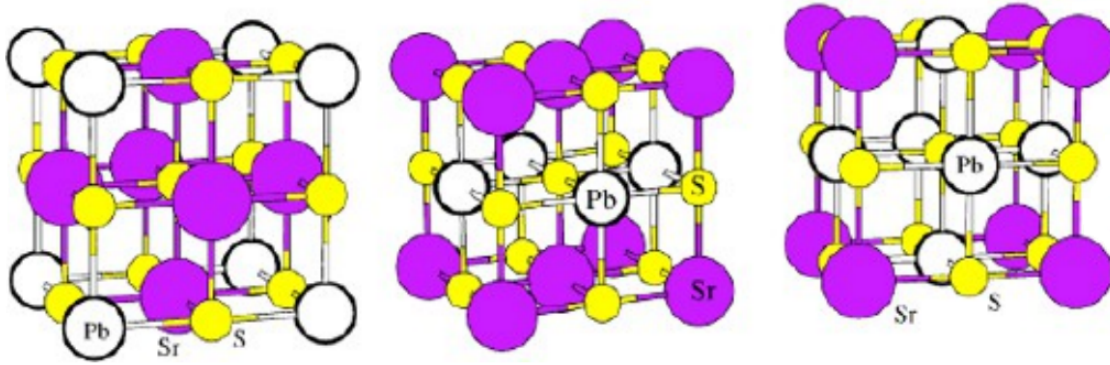


FIGURE 1.5: The input structure in the cluster expansion method is the rocksalt structure [3].

$$E = V_0 + \sum_i V_i \sigma_i + \sum_{i,j} V_{ij} \sigma_i \sigma_j + \sum_{i,j,k} V_{ijk} \sigma_i \sigma_j \sigma_k + \dots = \sum V_\alpha \phi_\alpha \quad (1.1)$$

V are the expansion coefficients and they are called ECIs (i.e. effective cluster interactions). They represent the contribution of each group of atoms, called cluster [6]. ϕ_α is called the correlation function of cluster α [7]. If the number of ECIs is equal to the number of structures, then the ECIs can be determined analytically. In case there are less ECIs than structures, the least square method or linear programming can determine the optimal ECIs.

The clusters in equation 1.1 were not chosen beforehand. They were chosen in a way that a small number can reconstruct the configurational dependency of the energy; only the most important interactions are taken into account. Wolverton et al. employed Alloy Theoretic Automatic Toolkit (ATAT) [8]. For the Ca-Pb-S structure, 10 reaction coefficients were used in equation 1.1. For Sr-Pb-S, 21 coefficients were used. The accuracy of the model can be validated by predicting the energy of a structure that was not in the training set (the set of structures used for the fitting of the model). An accuracy of 5.5 meV/cation and 5.3 meV/cation was found for Ca-Pb-S and Sr-Pb-S.

Cluster expansion is well established nowadays, but there are some limitations to the method. For the results to be reliable, the interactions should depend on concentrations in a nonlinear way. The ECIs in equation 1.1 are concentration-independent however. In Ref. [9], a solution for this problem was proposed.

1.1.2.2 Database searching

A second way to determine relevant crystal structures is by using experimental information of chemically similar crystals. This is the method used in this thesis. In the case of the Pb-Bi-Po and Pb-Bi-Te phase diagrams, all experimentally observed binary and ternary crystals in group IV, V and VI of the PSE with a different stoichiometry or space group should be taken into

account. Replacing all original elements by Pb, Bi and Po/Te depending on which group in the PSE they belong to, one finds a set of crystal candidates. Replacing the original elements by Pb, Bi and Po/Te, which are in the sixth period (see figure 1.6), will lead to a volume increase. The influence of a variation in the ratio of the lattice parameters is also examined. Afterwards, the atomic positions should be relaxed towards their lowest-energy positions in order to get a meaningful result.

6 C Carbon 12.0107	7 N Nitrogen 14.00674	8 O Oxygen 15.9994
14 Si Silicon 28.0855	15 P Phosphorus 30.973761	16 S Sulfur 32.066
32 Ge Germanium 72.61	33 As Arsenic 74.92160	34 Se Selenium 78.96
50 Sn Tin 118.710	51 Sb Antimony 121.760	52 Te Tellurium 127.60
82 Pb Lead 207.2	83 Bi Bismuth 208.98038	84 Po Polonium (209)

FIGURE 1.6: Group IV, V and VI of the PSE. Original crystal elements should be replaced by Pb, Bi and Po/Te.

In Ref. [2], the phase diagram of Al-Zn-O is determined with this method. A number of crystals in the Al-Zn-O phase diagram were already observed experimentally. The diagram in figure 1.3 was found. Most of the compositions that were found were on the line that connect ZnO with Al_2O_3 , which means that the formation enthalpy of the crystals on this line should be derived with respect to the formation enthalpy of these two binary phases instead of the elementary crystals.

1.1.2.3 Unbiased structure prediction

Structure prediction is a metaheuristic method, meaning that there are no assumptions made (in contrast to the earlier discussed methods of cluster expansion and database searching) towards the problem. The whole space of possible crystal structures will be scanned leading to an unbiased solution [2]. In Ref. [10], Pickard et al. describe a method to search the PES for minima with DFT, called Ab Initio Random Structure Searching (AIRSS). This algorithm is not trivial, since the number of minima (and the computational cost) in the PES increases exponentially with the size of the system. The method starts by calculating random structures (with reasonable density), i.e. random points on the PES. Only sensible initial structures are considered, i.e. structures where the initial atom positions are not too close to each other. The PES will never have a minimum in the neighbourhood of such a configuration. The initial configurations are relaxed while symmetry and experimental constraints are conserved. The search is not exhaustive and therefore one cannot be sure that the global minimum has been found. The searches are

stopped when the same minimal-energy structure has been found multiple times. This is justified as the different initial structures have a wide variety.

Another structure prediction method is the genetic algorithm, which finds stable crystal structures using an evolutionary method similar to the process of natural selection. A random set of optimized structures is created, and the “fitness” of each structure is determined. In this case, the crystal characteristic that determines this fitness is the formation energy. Crystals with the lowest formation energy are recombined and mutated in order to find more stable structures in each new generation. The mutations consist of a perturbation in atomic positions, a perturbation of the lattice parameters, addition or removal of atoms and interchanging of atomic locations. The genetic algorithm allows a lot of freedom in the approach. E.g. the likeliness of reproduction for a certain crystal can be probabilistic according to its fitness, or a set of crystals with a fitness over a certain threshold can be chosen to have the same probability of reproduction. The chosen approach will influence the investigated area of the total solution space. Allowing only the structures with the lowest formation energy to reproduce will lead to fast convergence, but only similar crystal structures will be examined. Also allowing less stable structures to reproduce will increase the solution space and convergence time. The best crystal structures of each generation will usually be copied to the following generation, hence preventing loss of already discovered stable crystals. Once the most stable structure no longer changes for a certain predetermined number of generations, the cycle will halt [2, 11].

In Ref. [11], Tipton et al. use a genetic algorithm on the ternary Zr-Cu-Al phase diagram to determine its accuracy, and to determine the accuracy of the embedded atom model (EAM) that is available for this system. In the EAM, the energy of a crystal is written as a sum of functions of the distance between an atom and its neighbours. Formation energies are determined by the EAM, and the stable structures found by the genetic algorithm are afterwards recalculated using first principles as comparison. The genetic algorithm is able to determine most experimentally known stable structures. No new stable structures are found. This study proves the reliability of the used genetic algorithm as well as the EAM for this system.

1.2 Relevance of the Pb-Bi-Po phase diagram for MYRRHA

1.2.1 Introduction to MYRRHA

The MYRRHA project (figure 1.7) involves a relevant application of the Pb-Bi-Po phase diagram. This project is conducted at SCK•CEN, a study centre for nuclear energy in Mol, Belgium. With the MYRRHA project, the centre has the goal to boost technological advancement in the development of generation IV nuclear fission reactors by supporting scientific research. MYRRHA stands for Multi-purpose hYbrid Research Reactor for High-tech Applications. These different purposes include [12]:

- **Sustainable fission energy:** a demonstration of the physics and technology of an Accelerator Driven System (ADS) for transmuting long-lived radioactive waste.
- **Sustainable energy:** development of a fast spectrum reactor and fusion technology.
- **Enabling technologies for renewable energies:** the production of neutron-irradiated silicon.
- **Health care:** the production of radio-isotopes for nuclear medicine.
- **Science:** the fundamental research for the generation of new expertise in various fields.

1.2.2 Nuclear reactors

Nuclear reactors initiate and sustain a nuclear chain reaction in a controlled way. The heat released from this exothermal process will be absorbed by a coolant running past the reactor. A gas, water, molten salt, or in the case of MYRRHA: a liquid metal, can be used as coolant. This coolant will transfer the heat in order to generate steam in turbines. There exist reactors that transfer the heat directly to the water for the turbines without a coolant.

In commercial nuclear reactors, the exchange of heat between reactor and coolant is efficient. A disadvantage is the large quantities of uranium that are necessary. About 98% of uranium is not used in the reaction, because the ^{235}U concentration is subcritical if it drops below 1%. A solution is to no longer slow down the excess neutrons. In this way, ^{238}U , which is not easily fissioned [13], can be transmuted to ^{239}Pu which is fissionable. The efficiency of these reactors is much higher.

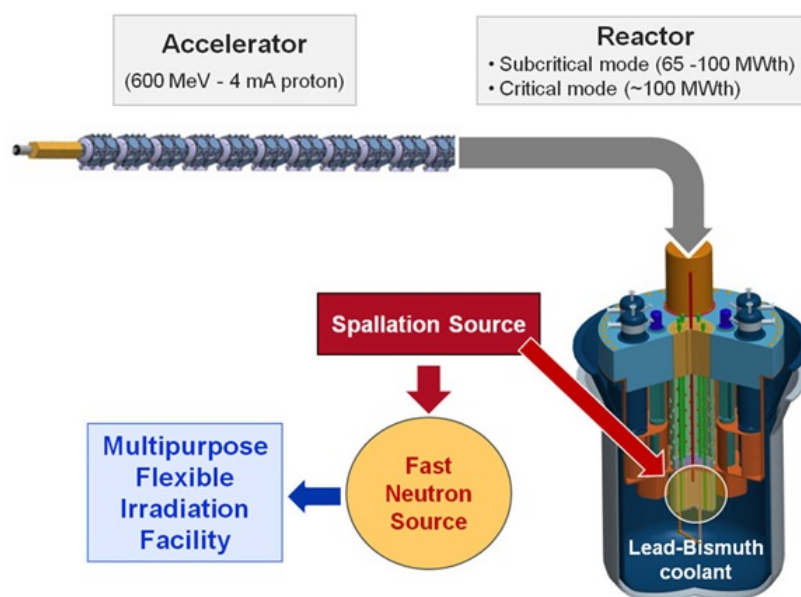


FIGURE 1.7: Visualisation of MYRRHA at SCK•CEN [12].

Coolants in these so-called fast reactors need to meet a set of requirements [2].

- A good thermal conductivity is needed.
- There shouldn't be any reaction moderation behaviour.
- The melting temperature is low: there is no solidification, and there is a high temperature difference over the core which leads to a more efficient heat extraction.
- The boiling point is high (the formation of gas bubbles should be stopped).
- Viscosity should be low.
- Chemical reactivity should be low.
- Neutron activation should be low.
- It should be transparent: in this way visual inspection of the internal reactor is possible.
- It should not be too expensive.

1.2.3 MYRRHA: a generation IV reactor

The MYRRHA reactor is hybrid in several ways. One of the reasons is that it contains a nuclear reactor as well as an accelerator. Spallation reactions can take place. In this type of reaction, a charged particle with very high kinetic energy is fired towards a stable nucleus. Due to this high kinetic energy (600 MeV for protons in MYRRHA) the charged particle (proton) will get trapped in the target nucleus. The excited nucleus will emit nucleons (about 10 to 20 neutrons in MYRRHA) and γ -photons. This leads to very high neutron fluxes [14, 15].

The coolant used in MYRRHA is the lead-bismuth eutectic (LBE) which is an alloy containing 55,5 % Bi and 44,5 % Pb. LBE has a couple of advantages which makes it superior to other coolant alternatives, e.g. Pb (which has a higher melting temperature) and N (higher reactivity with water and air and a lower boiling temperature) [16]. LBE scores well according to the earlier mentioned list of good coolant characteristics, and when compared to the alternatives Pb and N. In particular, the boiling temperature is very high (1943 ± 50 K), while the melting temperature is low ($397,7 \pm 0,6$ K) [17].

1.2.4 Po-contamination of LBE

LBE has a disadvantage that has to be taken into account for safety reasons. ^{209}Bi has a large cross section for neutron capture, which will transmute it into the highly radioactive α -emitter ^{210}Po .

Under normal working conditions of MYRRHA, a Po-concentration of only 1 ppm would be present in the LBE, which does not hinder the reactor. The Po that is formed by the transmuted Bi-atoms can form stable binary and ternary solidifying structures with Pb and Bi. Po that is contained within the LBE will decay after 100 days and will not cause any further problems. Po that escapes the LBE as a free atom or as a Po-containing molecule is however dangerous and filters are needed. It is key to know which stable molecules will be formed with Po and Pb or Bi. This was investigated by Rijpstra et al. in Ref. [18].

The goal of this thesis is to determine which stable crystals containing the elements Pb, Bi and Po can be formed at 0 K (since DFT is a ground-state theory; temperature dependency will not be introduced). If the formation enthalpy of the stable crystals is low enough, predictions can be made about the stability of these structures at the working temperature of the coolant (about 500 K). The formation of stable structures at this temperature will lower the volatile Po that escapes the LBE, and hence it will lower the needed capacity of the Po-filters.

Feuerstein et al. [19] investigated the evaporation behaviour of Po-210 in molten lead-lithium eutectic (Pb-(Li-17)) experimentally. The conclusion was that Po evaporates in the form of an intermetallic compound PbPo. PbPo is formed when Pb is heated (350°C) in Po-vapour. PbPo was reported to distil at 700°C [20]. The assumption that Po would form a stable compound with Pb was later confirmed by using Te as chemical substitute of Po [21]. Te was mixed at 0,01 wt% concentration with LBE. It preferentially formed PbTe, as was observed by the SEM technique. This experiment proves the existence of a stable (binary) Po-containing phase, which is up until now the only experimentally observed stable phase in the Pb-Bi-Po system.

1.3 Analogy between Pb-Bi-Po and Pb-Bi-Te phases

Te and, to a lesser extent, Se are generally considered as the chemical analogues of Po. On the other hand, Po resembles its horizontal neighbours Pb and Bi in its physical properties: it has a moderately high density and low melting and boiling point. It behaves as a typical metal (contrary to Te, which is a semiconductor) [20]. Due to the practical difficulties in experimenting with Po, it would be advantageous if one could prove a correspondence between the Pb-Bi-Po and Pb-Bi-Te phase diagram, e.g. a correlation of the formation energy of Po and Te, when substituted in the same crystal. Given experimental data of the Pb-Bi-Te phases, one could deduce the corresponding property of the analogue in the Pb-Bi-Po phase diagram. Such a correspondence was already demonstrated in Ref. [18], where a correlation between the solution enthalpies of Po and Te in LBE, elemental Pb and elemental Bi was found. These results are shown in figure 1.8.

The chemical similarity between Po and Te was employed in experimental studies. E.g. in Ref. [22] one investigates the removal of Po for Pb-Bi cooled fast breeder reactors by substituting

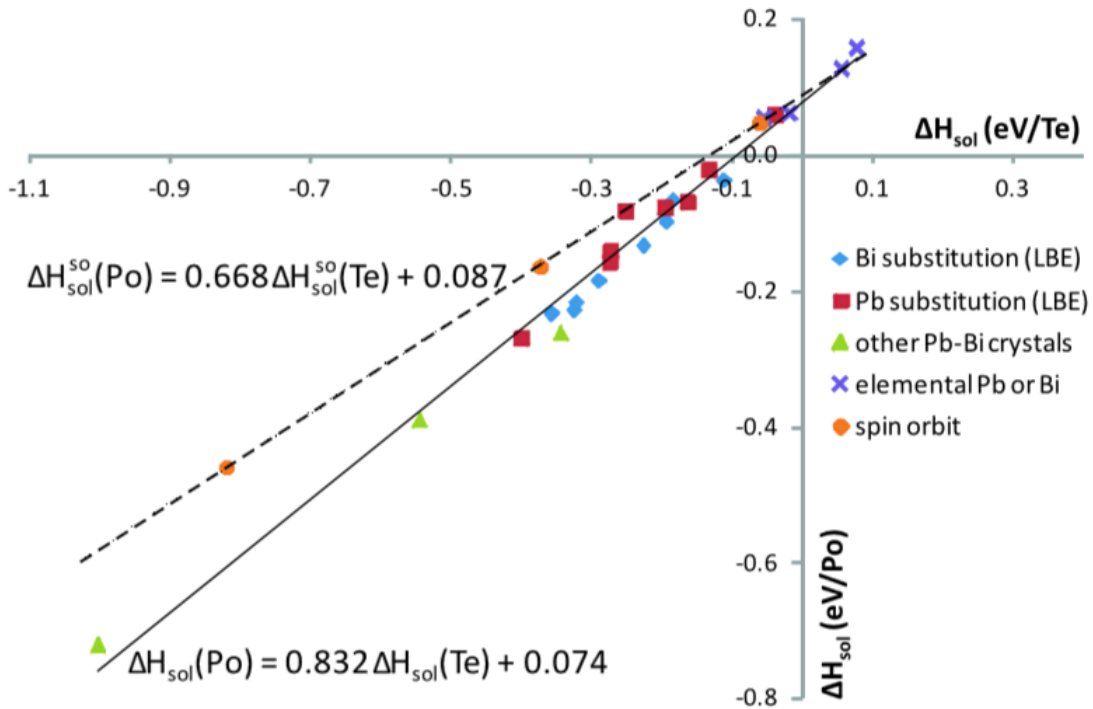


FIGURE 1.8: Correlation between the solution enthalpies of Po and Te in LBE (1/16), elemental Pb (various concentrations), and in elemental Bi (1/24). Additionally, the same correlation for full substitution of either Pb or Bi by Po or Te is given for PbBi (NaCl-structure) and for Bi_4Pb_3 . Every data point corresponds to a different local environment for Po/Te. In the two calculations that lead to every data point, all atomic positions were independently optimized (= the distance between Te and its neighbours is allowed to be different from the distance between Po and its neighbours). The dashed line is a similar fit through three well-separated data points, now taking spin-orbit coupling into account (from left to right: Bi-substitution in PbBi [NaCl], Pb-substitution in PbBi [NaCl]; 25% of Po/Te in fcc-Pb) [18].

PbPo by PbTe in order to speed up the experiments and to lower the financial cost. Other than the earlier mentioned similarity between Po and Te, there is not yet any experimental validation that the results of these experiments are transferrable between Po and Te. In this thesis, the correspondence between phases containing Po and Te respectively will be examined in chapters 4 and 5.

Chapter 2

Density Functional Theory

2.1 The many-body problem

The numerical results in this thesis are obtained using density functional theory (DFT) [23, 24], which is a method that solves quantum many-body problems in the ground state. A solid is such a many-body system: a collection of positive nuclei and negative electrons. Neglecting relativistic (spin-orbit) effects for now, the exact non-relativistic Hamiltonian for this system is given by:

$$\begin{aligned} \hat{H} = & -\frac{\hbar^2}{2} \sum_i \bar{\nabla}_{\vec{R}_i} M_i - \frac{\hbar^2}{2} \sum_i \bar{\nabla}_{\vec{r}_i} m_e - \frac{1}{4\pi\epsilon_0} \sum_{i,j} \frac{e^2 Z_i}{|\vec{R}_i - \vec{r}_j|} \\ & + \frac{1}{8\pi\epsilon_0} \sum_{i \neq j} \frac{e^2}{|\vec{r}_i - \vec{r}_j|} + \frac{1}{8\pi\epsilon_0} \sum_{i \neq j} \frac{e^2 Z_i Z_j}{|\vec{R}_i - \vec{R}_j|} \end{aligned} \quad (2.1)$$

Nuclei are situated at \vec{R}_i and have masses M_i . The electron positions are denoted by \vec{r}_i and have respective masses m_i . The first two terms of the Hamiltonian are the kinetic energies of nuclei and electrons. The last three contributions to the energy are the electrostatic interaction energy between nuclei and electrons, between electrons and electrons, and between nuclei and nuclei [25].

The eigenvalue equation of the time-independent many-body system (which is also called the time-independent Schrödinger equation) has following form:

$$\hat{H}\Psi(\mathbf{R}, \mathbf{r}) = E\Psi(\mathbf{R}, \mathbf{r}) \quad (2.2)$$

Solving this equation gives the eigenfunctions Ψ , which provide all possible information of the system.

2.2 The Born-Oppenheimer approximation

In order to solve the eigenvalue problem in equation 2.2, approximations are made. In the Born-Oppenheimer approximation one assumes that the speed of the nuclei is negligibly small when compared to the electronic speeds. Indeed, the mass of a proton (neutron) is about 1836 (1839) times the mass of an electron. When this ratio is multiplied with the atomic number Z (equal to 52, 82, 83 or 84 for Te-, Pb-, Bi- or Po-atoms) one can see that this is indeed a very feasible approximation. This has simplifying consequences for the Hamiltonian in equation 2.1. The first term disappears and the last term becomes constant. The rigid nuclei now act as an external electrostatic potential that will affect the electrons' movements. The nuclei only feel the mean field of the electrons due to their much slower speed. The decoupling of electronic and nuclear energy allows to write the eigenfunction as a product of an electronic and a nuclear eigenfunction.

$$\psi_{total}(\mathbf{R}, \mathbf{r}) = \psi_{nuclear}(\mathbf{R})\psi_{electronic}(\mathbf{R}, \mathbf{r}) \quad (2.3)$$

Each configuration of static nucleus positions corresponds to an energy eigenvalue. The collection of all nuclear configurations will determine the PES of the system. Consequently, solving the nuclear eigenvalue problem (dependent on the energy $U(\vec{R}_i)$ of the electronic eigenvalue problem) yields a set of energy levels corresponding to vibrations of the nuclei [26].

2.3 Density functional theory

Now that the Born-Oppenheimer approximation is introduced, the Hohenberg-Kohn theorem claims that the ground state density $\rho(\vec{r})$ of a many electron system is bijective with the external potential $V_{ext}(\vec{r})$ [24]. The ground-state density minimizes the electronic energy of the system. In order to find this minimal electronic energy, one introduces the Kohn-Sham-scheme (KS-scheme). It is a solvable, fictitious system that results in an electron density that is identical to the electron density of the real system. In this KS-scheme, a local internal potential replaces the mutual interactions from the original Hamiltonian. There exists a single Slater determinant wave function corresponding to the ground state density. The energy of this fictitious system consists of the contributions in equation 2.4.

$$E[\rho] = T_S[\rho] + \int d\mathbf{r} \rho(\mathbf{r})v(\mathbf{r}) + J[\rho] + E_{xc}[\rho] \quad (2.4)$$

The first term is the kinetic energy functional (corresponding to the KS-orbitals). It is defined as:

$$T_S[\rho] = \sum_{i=1}^N \langle \phi_i | -\frac{1}{2}\nabla^2 | \phi_i \rangle \quad (2.5)$$

The second term is due to the external potential of the static nuclei. It is defined by:

$$\int d\mathbf{r} \rho(\mathbf{r}) v(\mathbf{r}) = \sum_{i=1}^N \langle \phi_i | v(\mathbf{r}) | \phi_i \rangle \quad (2.6)$$

The third term is the Coulombic contribution of the electrons and can be written as:

$$J[\rho] = \frac{1}{2} \sum_{i,j=1}^N \langle \phi_i \phi_j | \frac{1}{|\mathbf{r}_i - \mathbf{r}_j|} | \phi_i \phi_j \rangle \quad (2.7)$$

The last term is the exchange-correlation energy, which is not known in practice, and one has to rely on approximations. In this thesis the PBE functional is used as approximation for the exchange-correlation term. PBE (named after Perdew, Burke and Ernzerhof) [27] is a generalized gradient approximation (GGA) functional [28–30]. This means that the functional depends on the density and the gradient of the density (in LDA or local-density approximation the latter is not taken into account). The PBE functional is one of the most accurate functionals when averaged over all properties. When one wants to predict a specific property it is usually best to use functionals that were specifically fitted to match that property. However this is not the case in this study, so PBE is a good choice.

All terms of equation 2.4 are now (approximately) known, and solving the KS-equations results in the corresponding eigenfunctions, i.e. the KS-orbitals. These orbitals don't have a physical meaning (except the HOMO which determines the ionization energy).

Periodic systems can be solved with DFT. Plane waves have to be used as basisfunctions. In this thesis the DFT-package WIEN2k [31] was used. WIEN2k uses the (linearized) augmented plane wave method, combined with local orbitals ((L)APW+lo) [32]. This method combines the good qualities of augmented plane wave (APW) and linearized augmented plane wave with local orbitals (LAPW+LO). The basis set can be a lot smaller when compared to LAPW; the rk_{max} -value (radius of the muffin tin sphere (MTS) multiplied with k_{max} , see section 2.5.2) in LAPW+lo can be about 1 smaller than the value in LAPW, and still nearly identical results are found. This results in a basis set that is only half the size of the one used in LAPW, and therefore in a computation time that is an order of magnitude smaller. The basis set is energy independent which keeps the eigenvalue problem linear [25].

2.4 Spin-orbit coupling

The reasoning up until now was correct for non-relativistic calculations. However, the relativistic effects will only be negligible for light elements. Pb, Bi and Po are heavy, and core electron velocities are more than half the speed of light. The non-relativistic Hamiltonian formulated in

equation 2.1 needs to be reformulated to account for relativistic effects. This was done in 1928 by Dirac [33] for spin $\frac{1}{2}$ -particles (such as electrons), three years after Schrödinger formulated the non-relativistic Hamiltonian. The Dirac Hamiltonian for an electron in a time-independent central potential $\phi(\vec{r})$ is given by equation 2.8:

$$H_D = c\boldsymbol{\alpha}\cdot\mathbf{p} + q\phi(\vec{r}) + \beta m_e c^2 \quad (2.8)$$

\mathbf{p} is the momentum operator, m_e is the electron rest mass. α_k and β are 4x4 matrices and are defined by:

$$\alpha_k = \begin{pmatrix} 0 & \sigma_k \\ \sigma_k & 0 \end{pmatrix}, \beta = I_4 \quad (2.9)$$

Where I_4 is the 4x4 unity matrix and σ_k are the Pauli-matrices defined by:

$$\sigma_x = \begin{pmatrix} 0 & 1 \\ 1 & 0 \end{pmatrix}, \sigma_y = \begin{pmatrix} 0 & -i \\ i & 0 \end{pmatrix}, \sigma_z = \begin{pmatrix} 1 & 0 \\ 0 & -1 \end{pmatrix} \quad (2.10)$$

The orbital angular momentum \mathbf{L} and the spin operator \mathbf{S} do not commute with the relativistic Hamiltonian and are no longer good quantum numbers. The total angular momentum $\mathbf{J} = \mathbf{L} + \mathbf{S}$ commutes with H as well as the helicity $\mathbf{S}\cdot\mathbf{P}$ (the projection of the spin along the direction of motion).

α_k and β are 4x4 matrices, hence the relativistic single particle wave function has four components.

$$\psi = \begin{pmatrix} \psi_1 \\ \psi_2 \\ \psi_3 \\ \psi_4 \end{pmatrix} = \begin{pmatrix} \Phi \\ \chi \end{pmatrix} \quad (2.11)$$

In equation 2.11, the wave function is rewritten as two spinors describing the spatial (Φ) and the spin (χ) degrees of freedom. The Dirac equation leads to two coupled equations for Φ and χ .

$$\begin{aligned} c(\boldsymbol{\sigma}\cdot\vec{p})\chi &= (\epsilon - q\phi - m_e c^2)\Phi \\ c(\boldsymbol{\sigma}\cdot\vec{p})\Phi &= (\epsilon - q\phi - m_e c^2)\chi \end{aligned} \quad (2.12)$$

We want to look at the non-relativistic limit of these coupled equations. This will decouple the equations in 2.12, and χ can be expressed in function of Φ . For the energy we take $E = E' + mc^2$ and we rewrite the central potential $q\phi(r)$ as V. After rewriting 2.12 we find for Φ :

$$(-c^2 \hbar^2 (\boldsymbol{\sigma} \cdot \nabla) \frac{1}{E' + 2mc^2 - V} (\boldsymbol{\sigma} \cdot \nabla) + V) \Phi = E' \Phi \quad (2.13)$$

We can expand $\frac{1}{E' + 2mc^2 - V}$ in powers of $\frac{(E' - V)}{2mc^2}$. If we take only the lowest orders into account, and approximate $E' - V(r)$ by $\frac{\mathbf{p}^2}{2m}$, we find the non-relativistic limit of the Dirac Hamiltonian.

$$H = \frac{\mathbf{p}^2}{2m} + V(r) - \frac{\mathbf{p}^4}{8m^3 c^2} + \frac{1}{2m^2 c^2} \frac{1}{r} \frac{dV}{dr} \mathbf{L} \cdot \mathbf{S} + \frac{\hbar^2}{8m^2 c^2} \nabla^2 V(r) \quad (2.14)$$

The first two terms in 2.14 correspond to the non-relativistic Hamiltonian (equation 2.1). The third term is the relativistic correction to the kinetic energy. The fourth term represents the spin-orbit interaction. The fifth term is the Darwin term and only affects the case $l=0$ [34].

Relativistic effects are most important for the core electrons as these move the fastest. WIEN2k will by default take full relativistic effects into account for the core electrons, i.e. inside the MTS. Outside the MTSs, only scalar relativistic effects are taken into account, which means that the spin-orbit coupling term in equation 2.14 is neglected. This term is indeed the most expensive to calculate computationally. In the scalar relativistic approximation the spin is still good a quantum number. Spin up and down states can be considered separately, and by combining them the basis set for spin up and down inside the atomic spheres can be constructed without much difficulty. This calculation is done by default for all atoms. When heavy atoms are considered (e.g. Pb, Bi and Po), the omission of spin-orbit coupling is no longer a good approximation. Full relativistic effects have to be introduced in all calculations in this thesis. Spin-orbit coupling is added in a perturbative way (otherwise it would be too computationally demanding for large systems). First the eigenvalue problem is solved in the usual way, i.e. separately for spin up and spin down states, for the Hamiltonian in 2.14 without the spin-orbit term.

$$\hat{H} \Psi_1 = \epsilon_1 \Psi_1 \quad (2.15)$$

In a second step the full Hamiltonian in of equation 2.14 is considered in a basis determined by the eigenfunctions of equation 2.15, which is usually a lot smaller than the original basis set. The spin-orbit term leads to non-diagonal matrix elements.

$$(\hat{H} + \hat{H}_{SO}) \Psi_2 = \epsilon_2 \Psi_2 \quad (2.16)$$

Electrons in the interstitial regions are not considered to be relativistic, and are calculated by the non-relativistic Hamiltonian in equation 2.1 [35, 36]. The three crystal regions mentioned in this reasoning are visualised in figure 2.1.

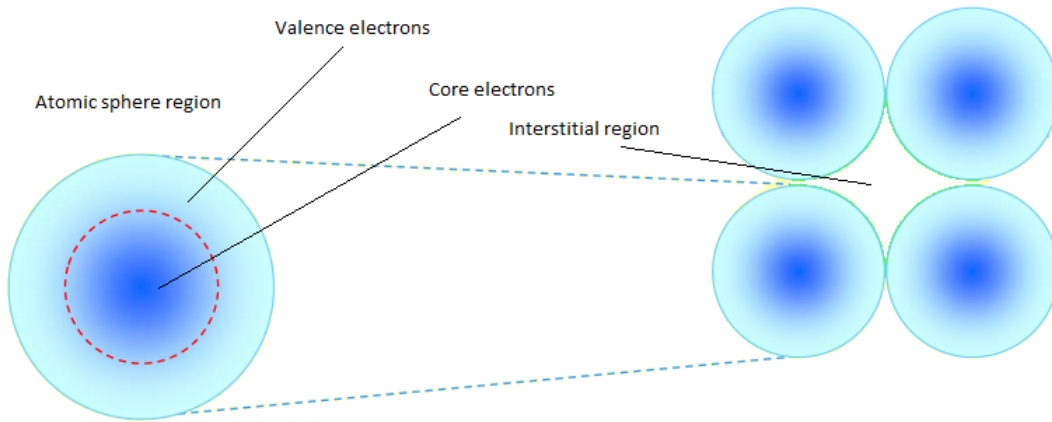


FIGURE 2.1: Scheme of the different crystal regions. Core electrons and valence electrons form the atomic sphere region or MTS region. All other space is interstitial space between the atoms [37].

2.5 WIEN2k parameters

An important topic that has to be taken into account before starting calculations in WIEN2k are the convergence criteria. These criteria contain the WIEN2k parameters rk_{max} , number of k-points and E_{max} . These will be discussed in this section without going into theoretical detail. The numerical value of these parameters in order to gain accurate results is determined in section 3.1.

A crystalline solid is periodic and hence a plane wave basis set is used. The Fourier transform of a plane wave is a single point in reciprocal space. The collection of all points that lead to a plane wave commensurate with the crystal lattice form the reciprocal lattice (in reciprocal space). Making use of Bloch's theorem [38] one can prove that the single particle wave function can be written as:

$$\varphi_{\vec{k}}^n(\vec{r}) = \sum_{\vec{K}} c_{\vec{K}}^{n,\vec{k}}(\vec{r}) e^{i(\vec{k}+\vec{K})\cdot\vec{r}}, \quad (2.17)$$

where \vec{k} is a wave vector inside the first Brillouin zone, and \vec{K} is a reciprocal lattice vector.

2.5.1 Number of k-points

The continuous wave vector \vec{k} in equation 2.17 requires discretisation to evaluate it computationally. The integral to calculate the density is replaced by following discrete sum [38]:

$$\rho(\vec{r}) = \sum_{\vec{k}} w_{\vec{k}} \sum_i n_{i\vec{k}} |\varphi_{i\vec{k}}(\vec{r})|^2, \quad (2.18)$$

where w_k are weight factors, and n_i are the occupation numbers of the Kohn-Sham orbitals. With increasing number of k-points, the result of the DFT-calculation should converge. There is a distinction between reducible k-points (the number of k-points that are given as input to WIEN2k) and the irreducible k-points. Due to symmetry of the unit cell, some reducible k-points are equal and don't have to be calculated again. The convergence of the calculation as a function of the number of k-points is summarized in 3.1.1

2.5.2 rk_{max}

In equation 2.17 there is a summation over all reciprocal lattice vectors. This summation is infinite and should thus be truncated. Higher \vec{K} -values will account for electrons with high energies. The WIEN2k parameter that corresponds to this truncation is rk_{max} , which is the maximal \vec{K} -vector multiplied by the radius of the MTS. This radius determines in which region the electrons are described by atomic-like functions (inside the spheres) or plane waves (outside the spheres). In the calculations in this thesis it is equal to 2.5 au for all calculations. Due to the MTS-radius being constant, the rk_{max} value can be constant too in order to get equal basis sets. Comparison of crystals calculated with unequal basis sets would not lead to accurate results. Convergence of rk_{max} is tested in section 3.1.2.

2.5.3 E_{max}

In equation 2.16 a matrix diagonalization is performed in the basis set of the non-perturbed eigenvalue equation. This means that the spin-orbit effect has to be small in order for this to work. When this is not the case, extra eigenstates from the first eigenvalue problem have to be taken into account. This can be done by increasing the E_{max} -parameter. It is defined as the maximal energy for which the eigenvalues are calculated. Convergence tests of this parameter are summarized in 3.3 [39, 40].

Chapter 3

Methodology

3.1 Convergence tests

In this section the convergence of the three WIEN2k parameters mentioned in 2.5 (number of k-points, $r_{k_{max}}$, and E_{max}) will be discussed. Due to the heavy elements and possible complex structures in the Pb-Bi-Po and Pb-Bi-Te phase diagrams, calculation speed will be an important factor in the choice of correct parameters.

Numerical precision will be tested in a relative way. When one wants to calculate e.g. formation energies, only energy differences matter. Convergence requirements will be less strict when compared to absolute convergence. In the three convergence tests, the energy difference between an undeformed unit cell and an expanded unit cell (with a volume expansion of 4%) is determined for different values of the parameters. It is assumed that convergence is achieved when the maximal tested parameter value is reached. In this way the convergence results can be plotted in an accessible way.

The crystals Pb, Bi, Po, Te, Bi_2Te_3 and Bi_2Po_3 were tested for convergence. It is assumed that the results are applicable to all binary and ternary phases in the Pb-Bi-Po and Pb-Bi-Te phase diagram. This is a reasonable assumption, as the interatomic distances and the gross features of the interaction between the constituting elements are similar in all these materials. When one parameter is tested, the other two are fixed. This is acceptable because these parameters are only very slightly coupled. The default parameters are: number of k-points=5000, $r_{k_{max}}=8,5$ and $E_{cut}=E_F+5.0$ Ry.

3.1.1 Number of k-points convergence test

The number of k-points is varied over the values 1000, 2000, 5000, 10000 and 20000. These are dependent on the volume of the unit cell. Smaller unit cells require more k-points: the number

of k -points is inversely proportional to the volume. Indeed, in reciprocal space the volume of the first Brillouin zone is inversely related to the volume of the unit cell in real space [38]. For this reason the graphs in this section are scaled: the number of k -points for a crystal (X) is arbitrarily given with respect to the volume of the Pb unit cell:

$$N'(X) = \frac{V(\text{Pb})}{V(X)}N(X), \quad (3.1)$$

where $N'(x)$ is the normalised number of k -points, N is the number of k -points, and $V(X)$ is the unit cell volume of crystal X . The energy axis is scaled so that the energy error per atom is given. Figure 3.1 summarizes the results of the relativistic calculation.

The energy errors oscillate but become gradually smaller as the number of k -points increases. The convergence is not variational [41]. The results show very good convergence even for the lowest number of points tested. The number of k -points for convergence will be chosen as 5000 for a Pb unit cell, i.e. $184.000/\text{\AA}^{-3}$. The numerical precision is better than 0,3 meV for all crystals for this value.

3.1.2 rk_{max} convergence test

The rk_{max} -values are varied from 5 to 10 with steps of 1. Convergence is variational which means that errors will get increasingly smaller with increasing rk_{max} . The results are summarized in figure 3.2.

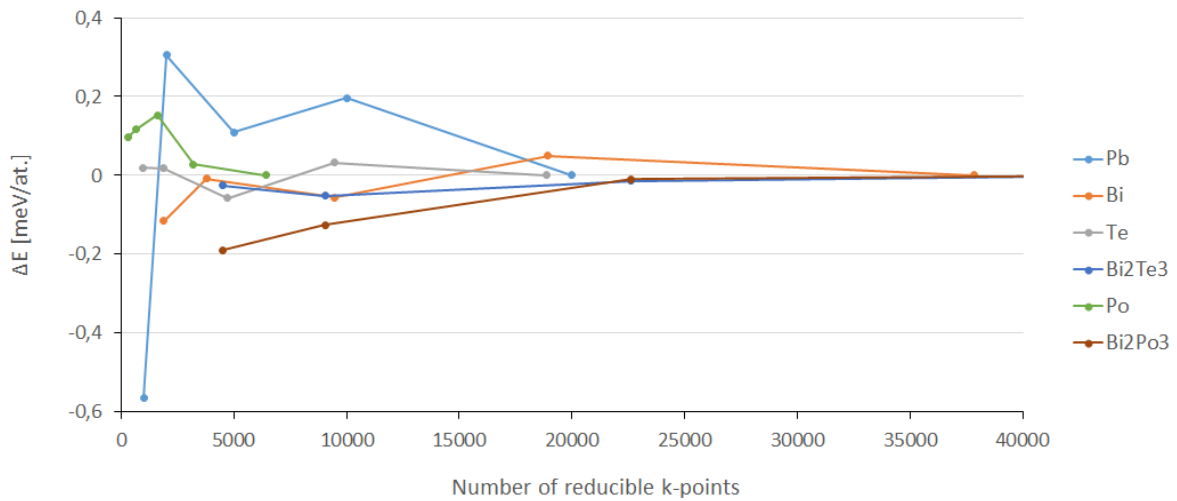


FIGURE 3.1: Graph of the convergence of number of k – points. The x-axis is the normalized number of k – points according to equation 3.1. The y-axis is the energy error per atom.

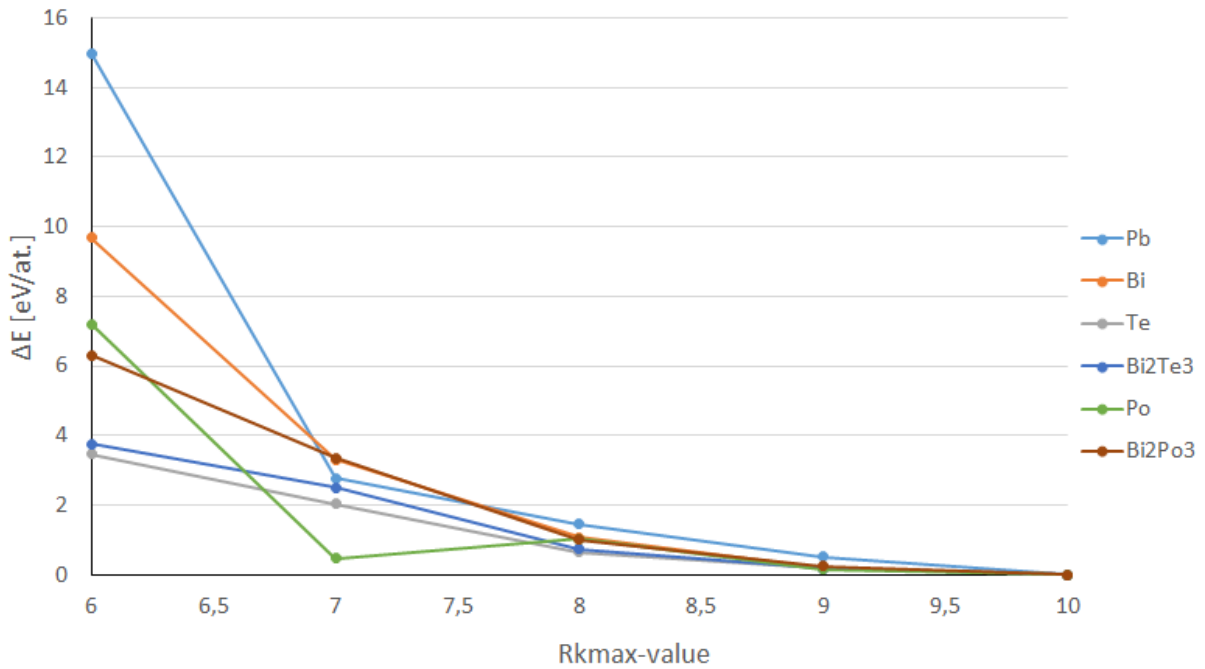


FIGURE 3.2: Graph of the convergence of rk_{max} -value. The x-axis shows the rk_{max} -value. The y-axis is the energy error per atom.

The errors in figure 3.2 are an order of magnitude larger than in figure 3.1. The rk_{max} -value is hence the determining factor for the accuracy (in non-relativistic calculations, where E_{max} is not taken into account). In order to get the same accuracy as for the k-point convergence test, an rk_{max} -value of 9 is needed. Computational complexity increases exponentially with increasing rk_{max} -value. This value is too large to be computationally feasible in the allotted time. A value of 8 was chosen, which leads to calculations that are approximately ten times less demanding. The error of ± 2 meV/atom does not cause a problem: this is small enough to determine formation energies with sufficiently high accuracy.

3.1.3 E_{max} convergence test

The convergence of E_{max} was tested by varying the energy from 5 to 10 Ry above the Fermi energy (E_F) with steps of 1 Ry. A gradual convergence is not visible in figure 3.3. This is remarkable, since the spin-orbit contribution is calculated in a variational way. The error margins remain nevertheless in reasonable margin (± 3 meV/atom) for E_{max} -values of E_F+7 Ry and higher. This energy of E_F+7 Ry will be used in further calculations. If the errors of all three convergence tests are summed, one gets a calculation precision of ± 5 meV/atom.

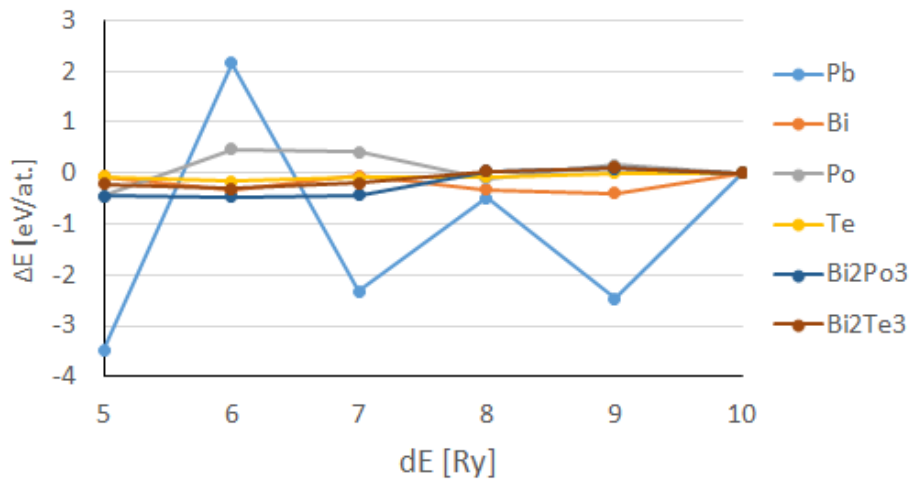


FIGURE 3.3: Graph of the convergence of E_{max} -value. The x-axis shows the E_{max} -value. The y-axis is the energy error per atom.

3.2 Calculation scheme

The investigated crystals originate from experimental data. Substitution of certain elements by the larger Pb-, Bi- and Po/Te- atoms will lead to a volume increase of the unit cell. The unit cell enlargement will be calculated using the Birch-Murnaghan equation of state (EOS). In a second step, the atomic positions will be varied until the geometry is found where the forces on the atoms are minimized. In a third step, the ratio of the unit cell parameters will be varied until a minimum in total energy is found. In a fourth and last step, the atomic positions are again optimized, as was the case in step 2. These steps will be discussed in following sections 3.2.1, 3.2.2 and 3.2.3.

3.2.1 Volume optimization

Because we did not find a simple way to make a rough estimate of the volume of a Pb-Bi-Po-crystal without an actual DFT calculation, we chose to estimate the starting volume using low-accuracy DFT calculations. The equilibrium energy is determined by fitting a third order Birch-Murnaghan curve. The Birch-Murnaghan relation is an EOS where the energy is written as a function of the unit cell volume [42]:

$$E(V) = E_0 + \frac{9V_0B_0}{16} \left\{ \left[\left(\frac{V_0}{V} \right)^{2/3} - 1 \right]^3 + \left[\left(\frac{V_0}{V} \right)^{2/3} - 1 \right]^2 \left[6 - 4 \left(\frac{V_0}{V} \right)^{2/3} \right] \right\} \quad (3.2)$$

E_0 is the equilibrium energy, V_0 is the equilibrium volume, B_0 is the bulk modulus, and B_1 is its pressure derivative. A typical Birch-Murnaghan fit is shown in figure 3.4. The volume is varied with steps of 3% for all EOS calculations in this thesis.

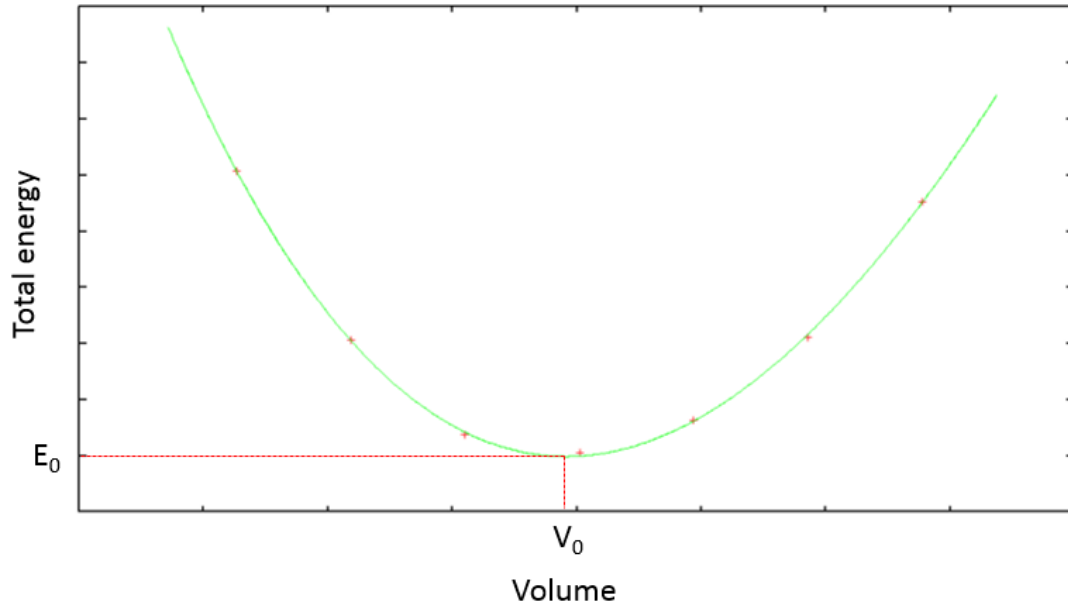


FIGURE 3.4: Third order Birch-Murnaghan fit.

3.2.2 Geometry optimization

After the equilibrium volume is determined, the atomic positions are varied until the forces acting on the atoms are reduced to the minimum. The MSR1a method is used. In this method, the densities and the atomic positions are treated as variables, and the self-consistent solution for the densities and gradients are found simultaneously. This is in contrast to a standard double loop position optimization scheme, where the energy and forces are calculated after a normal self consistent field (scf) cycle, and the next more stable configuration is guessed by moving the atoms according to the calculated forces by a conjugate gradient method. The MSR1a and double loop method are schematically summarized in figure 3.5. The MSR1a method is variational; allowing the atoms to move makes the problem consequently easier to solve than the double loop method. MSR1a is a factor 1,5 to 4 faster for large test cases in comparison. The MSR1a code will gradually lower the energy. It is possible that a slight rise in the energy occurs due to large displacements of the atoms. In the next iterations the densities will be adjusted, lowering the energy [43].

3.2.3 Ratio optimization

A more stable unit cell can be found if the unit cell volume is kept constant, but the ratio of the lattice parameters is varied. This is not applicable to cubic unit cells. Unit cells where the lattice parameters a , b and c satisfy $a = b \neq c$ or $a \neq b \neq c$ could reach a more stable energy by optimizing the ratio of lattice parameters. In the first case, one needs to vary the a/b -ratio while keeping $b=c$. In the latter case one needs to vary a/b and a/c .

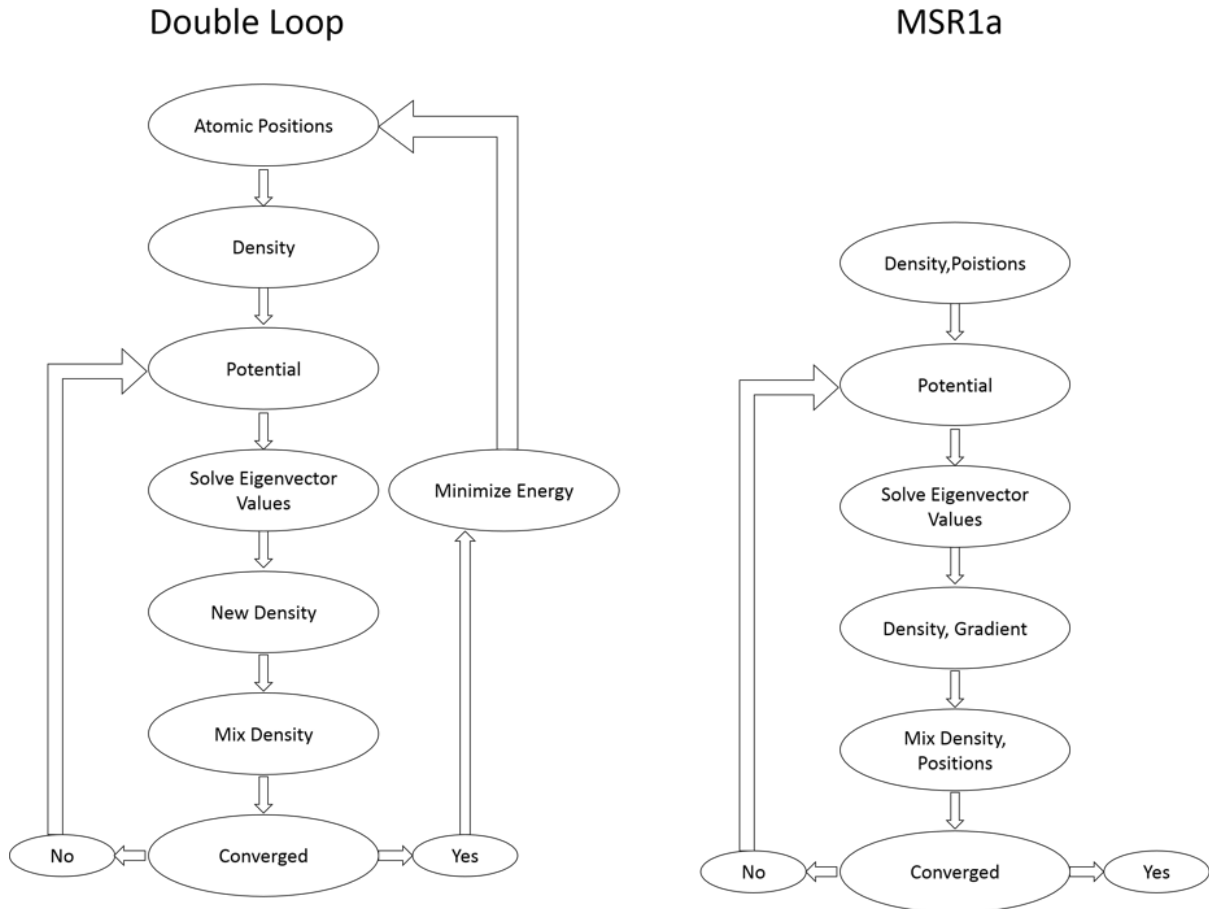


FIGURE 3.5: Schematical representation of the working principle of double loop optimization (left) versus MSR1a (right).

An example of this procedure where $a \neq b \neq c$ is given in figure 3.6. The investigated crystal is PbBi_2Po_4 , which has the orthorhombic Pnma -structure. The lattice parameters are each varied with a lattice parameter expansion of -2%, 0% and 2%. This gives $3^3=27$ different unit cell configurations, which are depicted schematically in the cube on the left side of figure 3.6. On the right side, three plots are given, corresponding to $c=-2\%$, 0% and 2% . The variation of the a and b is shown on the x - and y -axis respectively. One can conclude from these graphs that the energy will lower if a and c remain constant and if b decreases.

To determine the equilibrium parameters more precisely, one can fit a quadratic polynomial to these 27 data points, assuming that the equilibrium configuration is approximated sufficiently after volume and geometry optimization. The energy can then be written as:

$$E(a, b, c) = \alpha.a^2 + \beta.b^2 + \gamma.c^2 + \delta.ab + \epsilon.ac + \zeta.bc + \eta.a + \theta.b + \iota.c + \kappa \quad (3.3)$$

a , b and c are the lattice parameters. α , ..., κ are fitting parameters. The least-squares method is used for this fit. Afterwards the equilibrium point that has to be positive definite is determined. This algorithm is implemented in a script, using R [44]. Ratio optimization is done for

all binary and a couple of ternary phases, and the decrease of energy is always negligible when compared to the numerical precision of the DFT calculations. For this reason, this step (and also the last geometry optimization) are not calculated for all crystals. Furthermore, the omission of this step eliminates computational problems for triclinic and monoclinic crystals, where the additional degree of freedom in one or more angles of the unit cell would result in a huge amount of structures to be calculated.

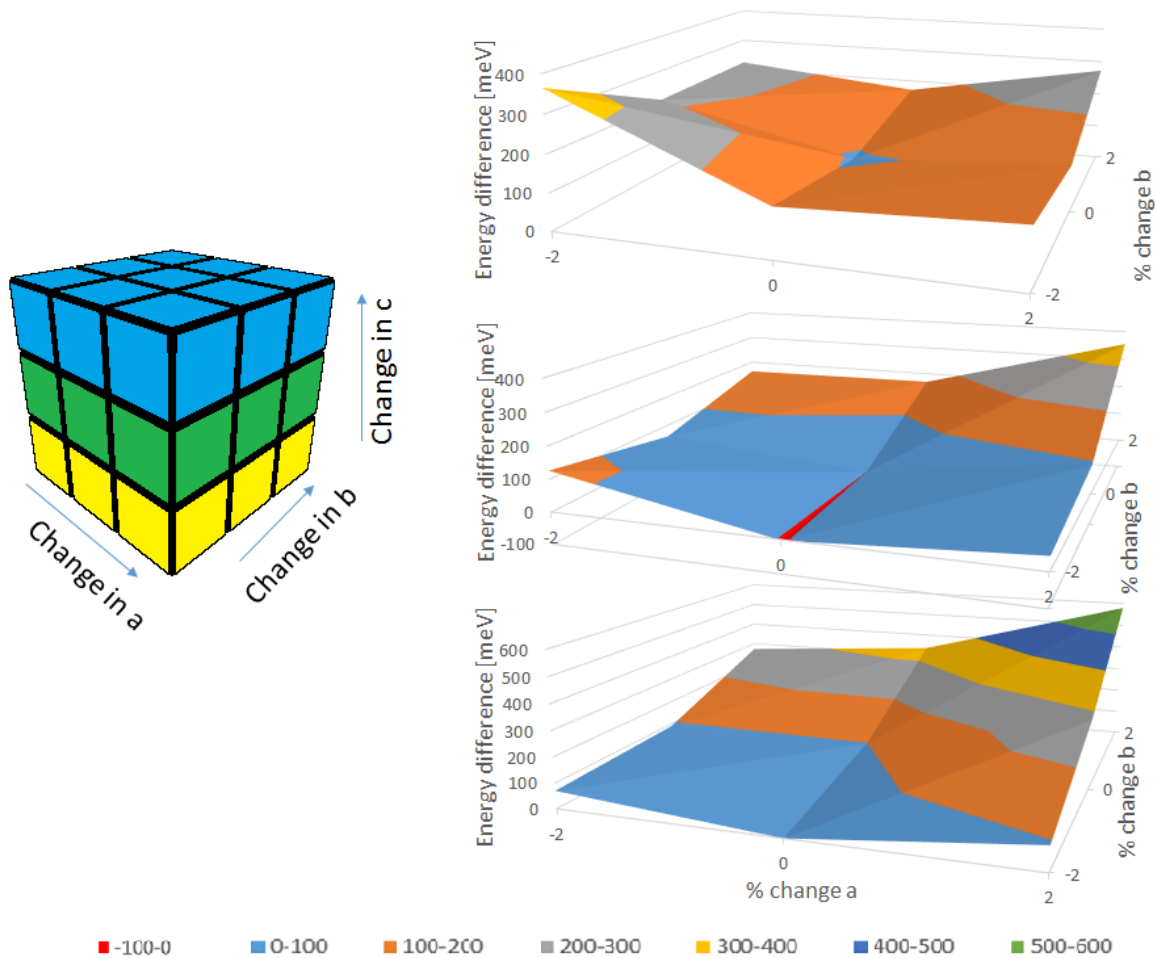


FIGURE 3.6: Graphical representation of the ratio optimization procedure for PbBi_2Po_4 . On the left: schematical representation of each of the 27 possible configurations. On the right: 3 plots corresponding to the c -parameter changed by -2% , 0% and 2% . The difference in total energy before and after ratio optimization is given. In the red region for $a=0$, $b<0$, $c=0$, the energy lowers, resulting in a more stable configuration.

Chapter 4

Binary Phase Diagrams Containing Pb, Bi, Po or Te

4.1 Introduction

The binary phases of Pb-Bi, Pb-Te, Bi-Te, Pb-Po and Bi-Po will be discussed in this chapter. There is experimental data available for the first three phase diagrams, which will be used to validate the results obtained by DFT. Furthermore, the correlation between Pb-Po and Pb-Te, and between Bi-Po and Bi-Te will be examined.

The investigated crystals originate from the binary experimental crystals with elements belonging to the fifth or sixth period of the PSE. This limits the otherwise huge number of possible element permutations (e.g. if also lower periods in the PSE would have been included) to only the most probable crystal structures. If a crystal structure were to be found that is more stable than any combination of earlier predicted elementary or binary crystals, the convex hull will be redrawn, with the possibility of removing crystals that were claimed to be stable earlier. Crystals above the convex hull are not stable, or metastable at best. The crystallographic data is extracted from the Inorganic Crystal Structure Database (ICSD).

4.2 The Pb-Bi phase diagram

Four crystals belonging to the Pb-Bi phase diagram are investigated. Information about these three crystals is summarized in table 4.1. The results of the DFT calculation, where the formation energy with respect to the solid elements is determined, are shown in figure 4.1. According to these DFT predictions, there is no stable binary Pb-Bi phase. All formation energies are positive and lie above the convex hull, which is a horizontal connecting solid Pb and Bi. One can compare this result with the experimental Pb-Bi phase diagram [45], see figure 4.2.

Original crystal	Space group	cif-nr.	New crystal
SnSb	$Pm\bar{3}m$	651575	PbBi
SnSb	$F\bar{4}3m$	53968	PbBi
SnSb	$R\bar{3}mR$	52294	PbBi
SbBi	$Cmca$	160382	PbBi

TABLE 4.1: From left to right: (1) Original experimental crystals, (2) corresponding space group, (3) index number of the CIF-file in ICSD, (4) crystal with substituted Pb- and Bi-atoms.

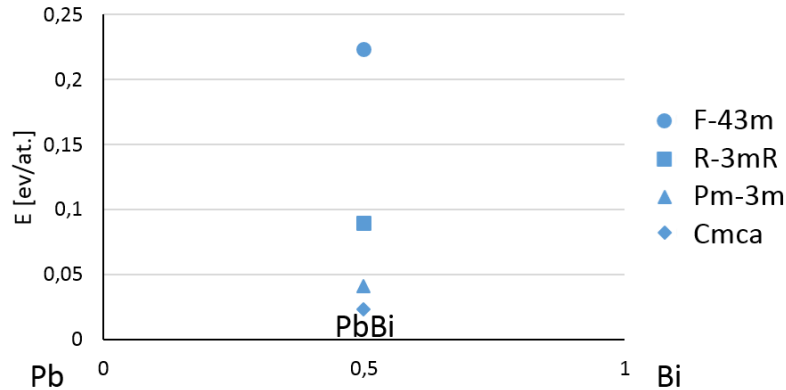


FIGURE 4.1: The Pb-Bi phase diagram, calculated from first principles.

If one looks at the ground state, one can see that there is no stable experimentally known Pb-Bi phase, which corresponds to the DFT results in figure 4.1. ICSD and Materials Project [1] also did not contain any experimental Pb-Bi phases (the three crystals were constructed solely from chemically similar crystals: SnSb), which is consistent with our DFT prediction.

4.3 The Pb-Te and Pb-Po phase diagram

Four crystals are investigated belonging to the Pb-Te and Pb-Po phase diagrams, and are summarized in table 4.2. The results of the DFT calculation are presented in figure 4.3. All three crystals have a negative formation energy with respect to the solid elements. The Te-containing crystals are more stable than the Po-containing crystals. This can be explained as follows. All original experimental crystals already contained Te, since there are no experimental crystals containing Po in ICSD. The substitution of Te by the bigger Po will lead to a less stable crystal. The $Fm\bar{3}m$ crystal structure is stable for both Pb-Te and Pb-Po. There is a clear visual correspondence between the formation energies of Pb-Te and Pb-Po. This correlation will be investigated in more detail in section 4.5.

Materials Project states that $Fm\bar{3}m$ is the most stable crystal structure, corresponding to the prediction in this thesis. The formation energy from Materials Project (calculated using VASP)

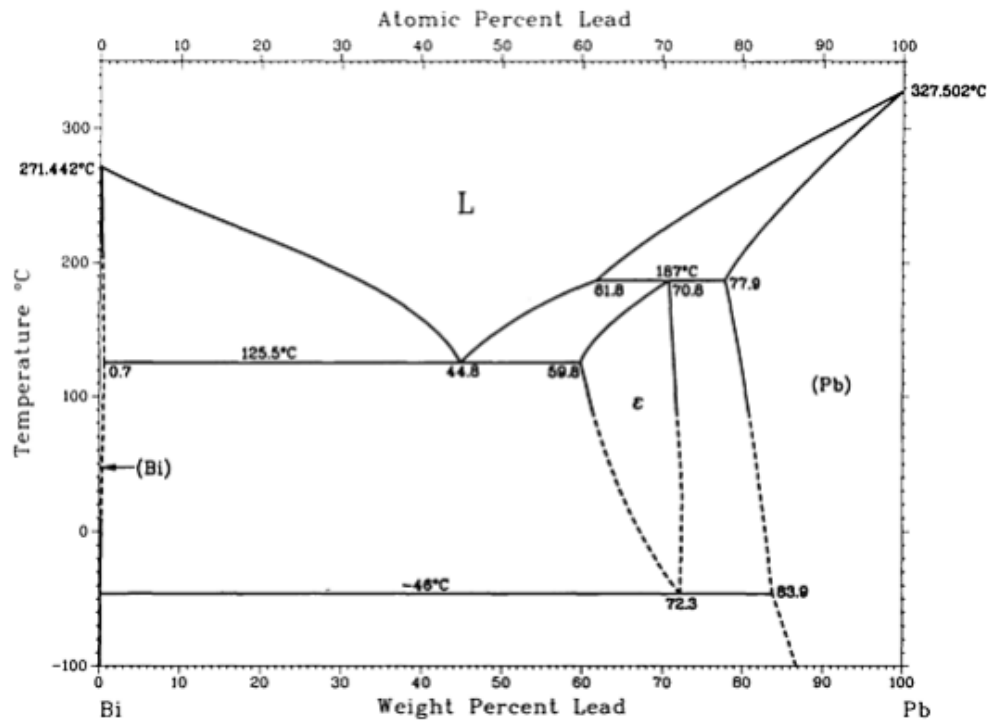


FIGURE 4.2: The experimental Pb-Bi phase diagram [45]. No experimentally stable phases in the ground state are known.

Original crystal	Space group	cif-nr.	New crystal
PbTe	Pnma	648582	PbPo/PbTe
PbPo	Fm $\bar{3}m$	105598	PbPo/PbTe
SnTe	F $\bar{4}3m$	53956	PbPo /PbTe
SnTe	Pm $\bar{3}m$	604129	PbPo/PbTe

TABLE 4.2: From left to right: (1) Original experimental crystals, (2) corresponding space group, (3) index number of the CIF-file in ICSD, (4) crystal with substituted Pb- and Po/Te atoms.

is -0,414 eV/atom. The value calculated using WIEN2k is -0,364 eV/atom. The formation energy from Materials Project is 0,050 eV/atom lower, a recurring overestimation when one compares this with the results in following section 4.4.

One can compare the result from first principles with experimental data. In Ref. [45] one mentions that there are two experimentally known stable structures at finite temperature: Fm $\bar{3}m$ and Pnma. These correspond to the two most stable structures obtained from first principles in the ground state. The energy difference between the most stable (Fm $\bar{3}m$) and the first experimentally existing metastable (Pnma) crystal is about 0,07 eV/atom. A similar number could be derived from figure 1.3, where ZnO₂ is a metastable industrially useful material that is somewhat more than 0,1 eV/atom above the convex hull [2]. Therefore, we can conclude that crystal

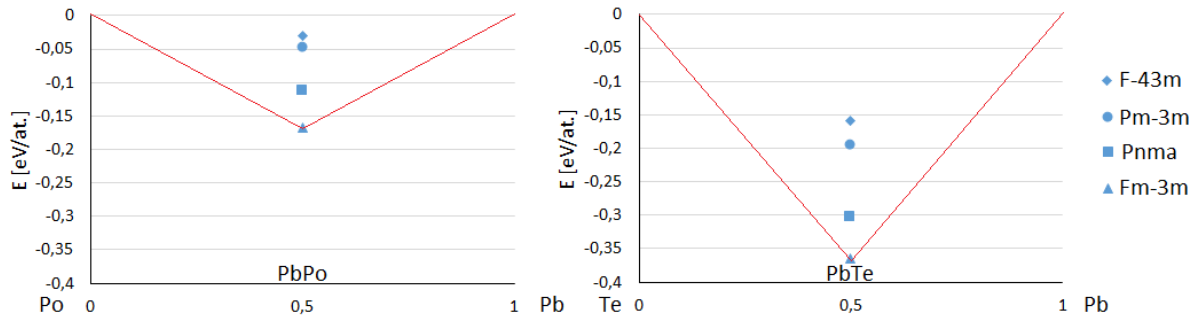


FIGURE 4.3: The Pb-Te and Pb-Po phase diagram, calculated from first principles.

structures that are within roughly 0,1 eV/atom above the convex hull cannot be ruled out as metastable crystals that can appear in nature.

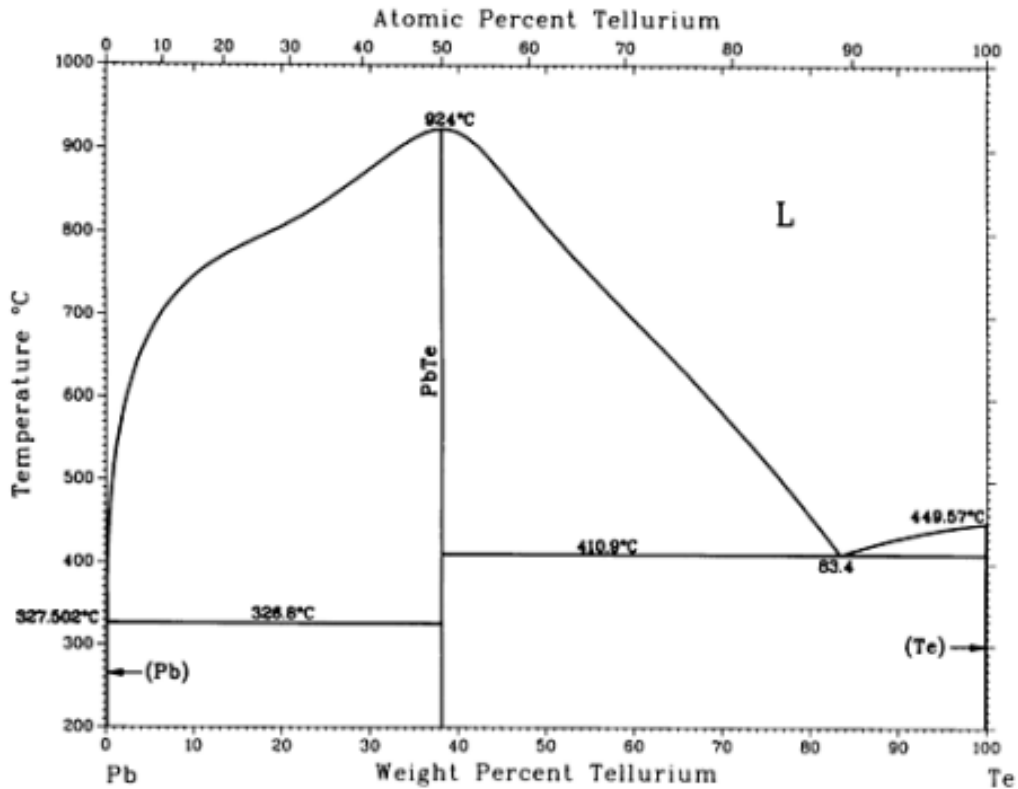


FIGURE 4.4: Experimental Pb-Te phase diagram. The PbTe phase in the $Fm\bar{3}m$ and Pnma crystals structure are stable in the ground state [45].

4.4 The Bi-Te and Bi-Po phase diagram

Eight crystals are investigated belonging to the Bi-Te and Bi-Po phase diagrams and are summarized in table 4.3. One crystal (BiPo in the Cmca space group) was added to the search group by accident, replacing the Sn atom by mistake by Te and Po, yielding an extra data point.

Original crystal	Space group	cif-nr.	New crystal
BiTe	Fm $\bar{3}$ m	44984	BiPo/BiTe
BiTe	Pm $\bar{3}$ m	617181	BiPo/BiTe
BiSn	Cmca	160382	BiPo/BiTe
Sb ₂ Te	P3m1	69557	Bi ₂ Po/Bi ₂ Te
Bi ₂ Te ₃	R3mH	20289	Bi ₂ Po ₃ /Bi ₂ Te ₃
Bi ₂ Te ₃	R $\bar{3}$ mR	15753	Bi ₂ Po ₃ /Bi ₂ Te ₃
Sb ₂ Te ₃	C12/c1	185954	Bi ₂ Po ₃ /Bi ₂ Te ₃
Bi ₄ Te ₃	R $\bar{3}$ mH	30526	Bi ₄ Po ₃ /Bi ₄ Te ₃

TABLE 4.3: From left to right: (1) Original experimental crystals, (2) corresponding space group, (3) index number of the CIF-file in ICSD, (4) crystal with substituted Bi- and Po/Te atoms.

The results of the DFT calculation are given in figure 4.5. As was the case for Pb-Te, all Te-containing crystals are systematically more stable than the Po-containing crystals. Four crystal structures turn out to be stable, both for Bi-Te and Bi-Po. The correlation between the results of Bi-Te and Bi-Po is again noticeable. The crystals that did not correspond to an experimentally known stable crystal (BiPo/BiTe (Cmca)) have the highest formation energy, which is an expected result.

The experimental Bi-Te phase diagram as published in Ref. [45] is shown in figure 4.6. This phase diagram shows several stable binary phases. For many of those, however, the crystal structure is not specified and cannot be found in the common crystallographic databases (ICSD, COD [46]). Only the phases for which the crystal structure is known, can be considered by DFT. The four stable crystal structures in figure 4.3 correspond to the experimental data [45].

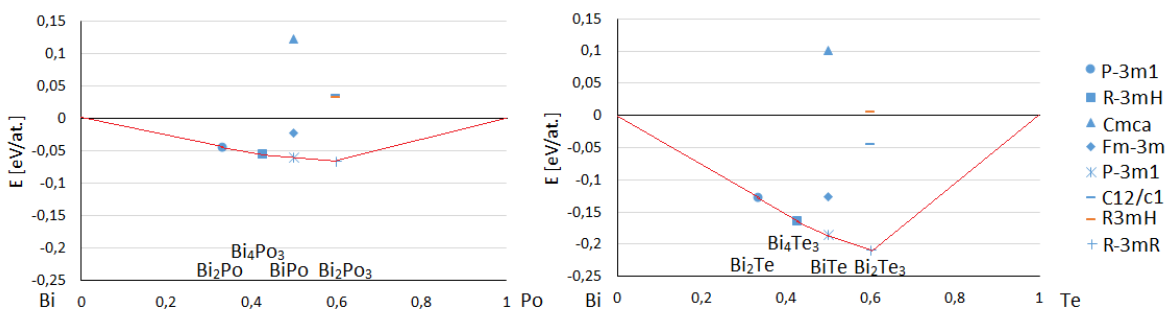


FIGURE 4.5: The Bi-Te and Bi-Po phase diagram, calculated from first principles.

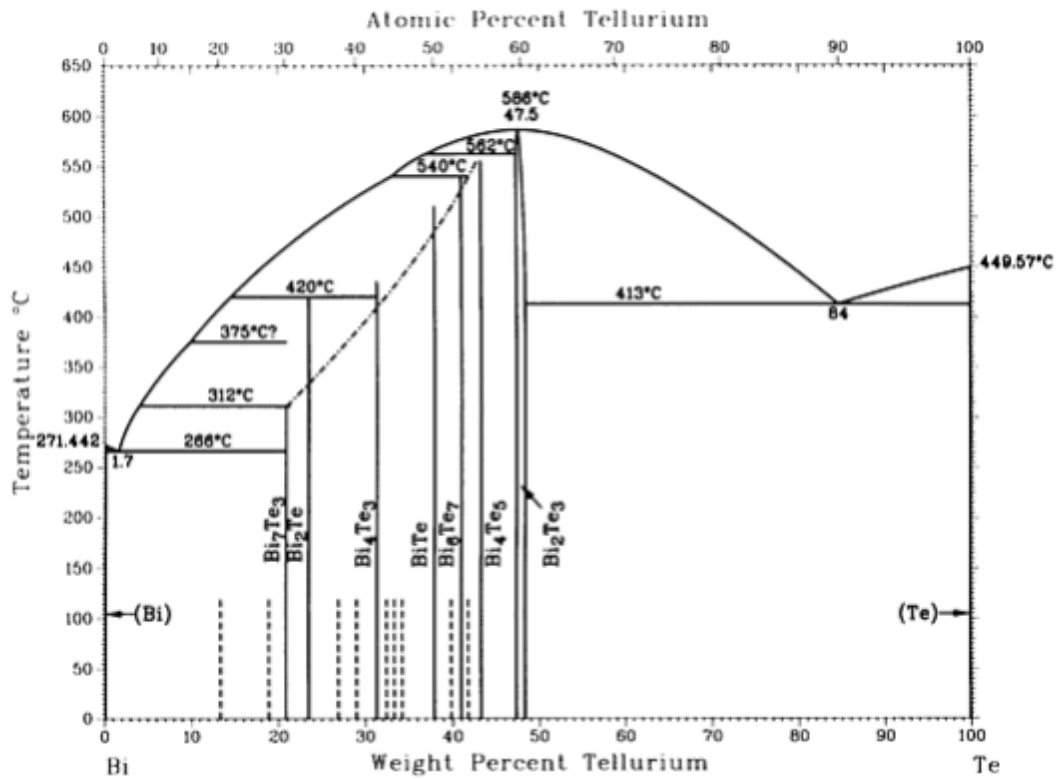


FIGURE 4.6: Experimental Bi-Te phase diagram [45].

Materials Project contains some information on the Bi-Te phase diagram. The phase diagram, calculated using VASP, is given in figure 4.7.

A quantitative comparison of the data obtained by WIEN2k and VASP is made in table 4.4. The stable PbTe crystal of section 4.4 is also added. Materials Project claims that Bi₂Te₃, Bi₄Te₃ and Bi₈Te₉ lie on the convex hull. This is in correspondence with the results obtained by WIEN2k: Bi₂Te₃ and Bi₄Te₃ are also stable. Bi₈Te₉ could not be calculated due to convergence problems. BiTe ($P\bar{3}m1$), stable according to the WIEN2k-calculation, lies 2 meV/atom above the convex hull according to VASP, a difference that can easily be attributed to calculation precision. One of the stable crystals according to WIEN2k, Bi₂Te, was not considered in the VASP-calculations. When one looks at the difference between the WIEN2k- and the VASP-data, one finds that VASP overestimates the formation energies for all crystals except for the unstable BiTe ($Fm\bar{3}m$). The root mean squared (rms) energy differences for the EOS between VASP- and WIEN2k results for the atoms Pb, Bi and Te equal 0,6 meV/atom, 0,4 meV/atom and 0,5 meV/atom respectively [47], small errors that do not explain the observed energy difference.

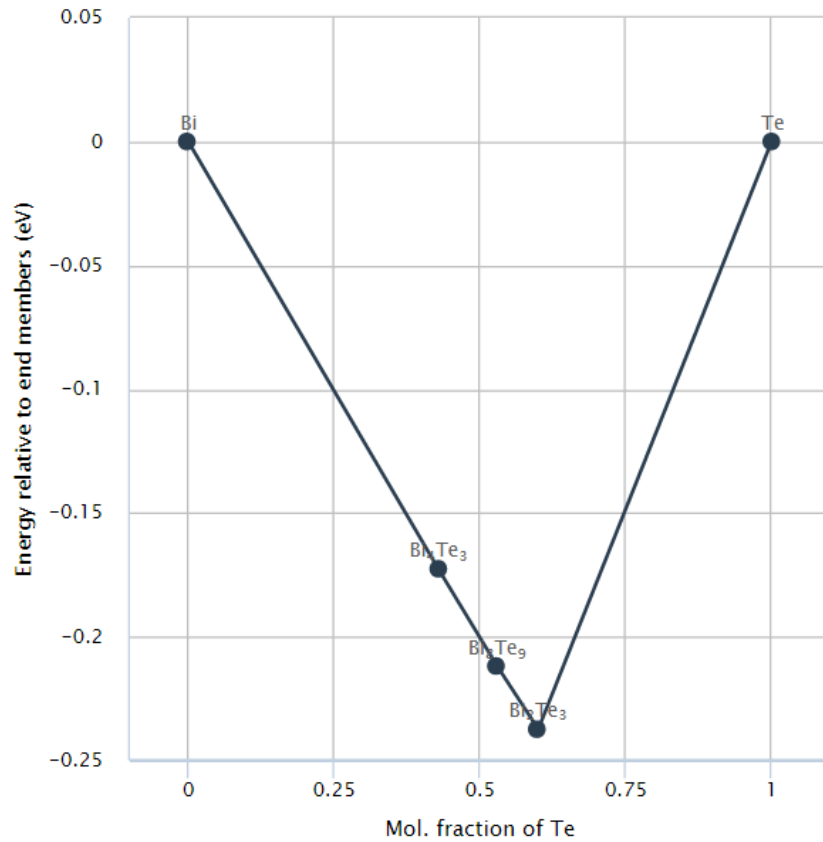


FIGURE 4.7: The binary Bi-Te phase diagram calculated by VASP, from Materials Project.

Formula	Space group	WIEN2k [eV/at.]	VASP [eV/at.] [1]	ΔE [eV/at.]
Bi ₄ Te ₃	R $\bar{3}m$	-0,165	-0,173	0,008
BiTe	P $\bar{3}m1$	-0,184	-0,199	0,015
BiTe	Fm $\bar{3}m$	-0,126	-0,069	-0,057
Bi ₂ Te ₃	R $\bar{3}m$	-0,209	-0,237	0,028
PbTe	Fm $\bar{3}m$	-0,364	-0,414	0,050

TABLE 4.4: Comparison of the data points of the Bi-Te and Pb-Te phase diagram, calculated by WIEN2K and VASP. From left to right: (1) Chemical formula, (2) corresponding space group, (3) formation energy calculated by WIEN2k, (4) formation energy calculated by VASP, (5) difference in formation energy between the WIEN2k and VASP calculations.

4.5 Correlation between binary phases containing Po and Te

The DFT calculations in sections 4.3 and 4.4 predict that all stable crystal structures for the Te crystals are also stable for the corresponding Po crystals, leading to the prediction of four stable phases in the Bi-Po phase diagram. This can be considered as a computational discovery: except for PbPo, which is experimentally known, nothing was yet known about other stable binary Po-containing phases.

The correlation between the binary phase diagrams containing Po and Te can now be investigated in a quantitative way. A trend is found if the formation energy per Po atom is plotted versus the formation energy per Te atom. In Ref. [18] a similar correlation was proven between the solution enthalpies of Po and Te substituted in an LBE matrix. The solution enthalpy for the substitution of x Pb (or Bi) atoms is defined by:

$$\Delta H_{sol} = [H(LBE + x.Po) + x.\mu_{Pb(Bi)}] - [H_{LBE} + x.\mu_{Po}] \quad (4.1)$$

The LBE-matrix is defined as hcp-Pb₈Bi₈, unstable (according to experimental phase diagram 4.2) and not calculated in this thesis. μ is the chemical potential, defined in these calculations as the formation energy per atom in the elemental solids. The formation energy in this thesis is defined by:

$$\Delta E = H(LBE + x.Po) - (8 - x).\mu_{Pb(Bi)} - x.\mu_{Po} \quad (4.2)$$

The three calculated data points using spin-orbit by Rijpstra et al. [18] correspond to the crystals PbPo (Fm3m), BiPo (Fm3m) and Pb₃Po (fcc). The formation energies of the first two crystals are also determined in this thesis. One can now work out four equations (for these two crystals, both with substituted Po and Te) that allow to determine $H(LBE)$, the only unknown in equation 4.1. Comparing equation 4.1 and 4.2 one can see that the offset one has to add for the two data points on both axes is given by:

$$\Delta E_{offset} = H_{LBE} - \mu_{Pb(Bi)} - \mu_{Pb(Po)} \quad (4.3)$$

The data point corresponding to Pb₃Po is formed by substitution in fcc Pb, for which definition 4.1 and 4.2 are the same, hence no offset has to be added. After these calculations, the results of this study can be compared with the correlation in this thesis and a good correspondence is observed. The results are visualised in figure 4.4. By least squares fitting, one obtains the following relation (the three data points by Rijpstra et al. are excluded):

$$\Delta E_{Po}[eV/at.] = 0,572 \cdot \Delta E_{Te}[eV/at.] + 0,050eV/at. \quad (4.4)$$

The determination coefficient R^2 of this correlation equals 0,96. An experimentalist could use relation 4.4 to predict the formation energy of binary Po phases, starting from experimental Te phases. In figure 4.9, the formation energies of the Pb-Po phase are plotted. The DFT results are compared to the predicted data starting from the analogous Te-containing phases. The same plot for Bi-Po is given in 4.10. Both figures show a good correspondence between the DFT formation energies and the formation energies determined using equation 4.4.

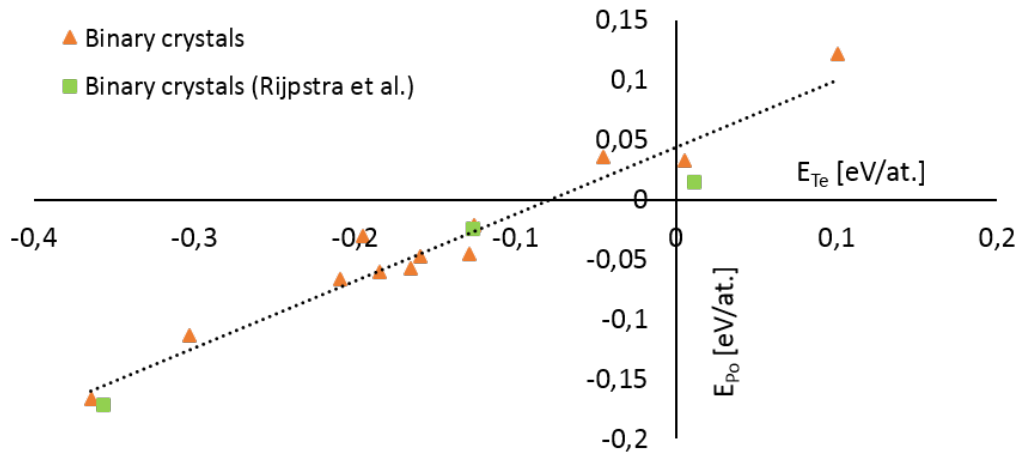


FIGURE 4.8: Correlation between the formation energy of Po and Te for the binary phases. The blue data points correspond to the binary phases calculated in this thesis. The orange data points correspond to the binary phases calculated by Rijpstra et al. in Ref. [18].

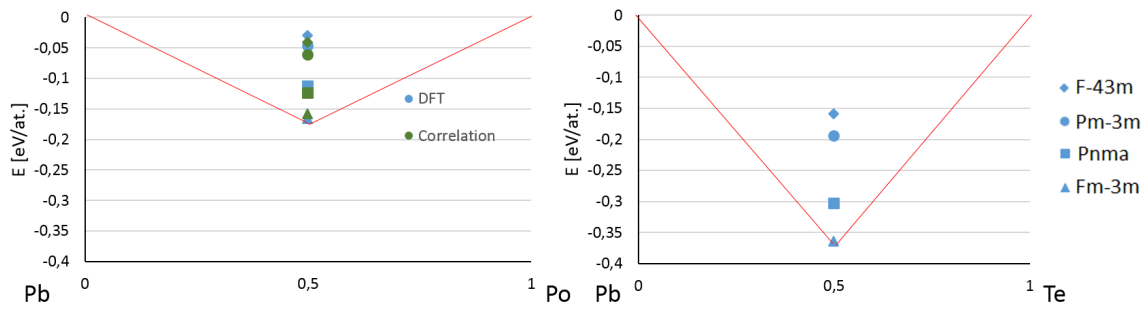


FIGURE 4.9: Comparison between the DFT results for the Pb-Po phase diagram and the results obtained using the correlation with the Pb-Te phase diagram.

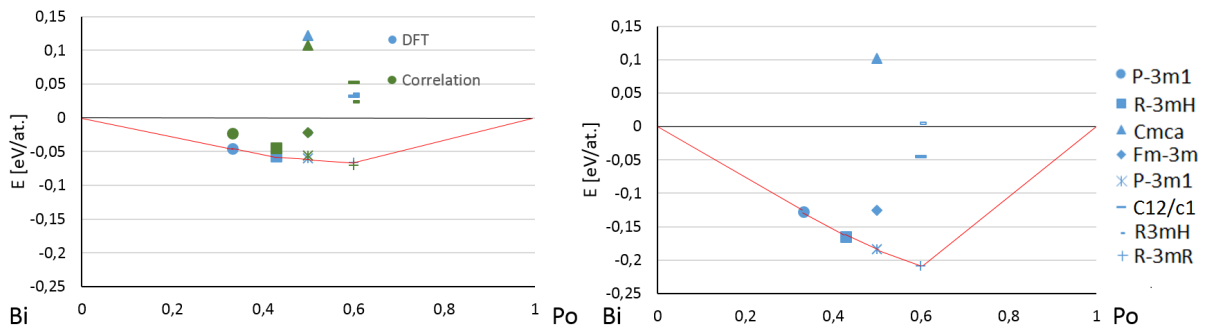


FIGURE 4.10: Comparison between the DFT results for the Bi-Po phase diagram and the results obtained using the correlation with the Bi-Te phase diagram.

Chapter 5

Ternary Pb-Bi-Te and Pb-Bi-Po Phase Diagrams

5.1 Introduction

The ternary Pb-Bi-Po and Pb-Bi-Te phases will be discussed in this chapter. The correlation between Po- and Te-containing ternary phases will be determined and compared to the data points of the binary phases calculated in chapter 4. The investigated ternary crystals originate from experimental crystals with elements belonging to period 3 to 6 of the PSE. The second period of the PSE was not included because of chemical dissimilarity between C, N, O and Pb, Bi, Po/Te respectively. All data is extracted from ICSD. Not all of these crystals were effectively calculated, however: in some cases the number of atoms in the unit cell was too large to be feasible within the timeframe of this work (e.g. with 72 atoms in the unit cell), while in other cases the geometry optimization took for yet not understood reasons ten times as long as common, making these cases unfeasible too. These problems lead to a reduction of the original search space from 33 crystals to 19 crystals. The fact that the total set of experimental crystals could not be investigated should not pose a problem. The method of only selecting crystals that have experimental chemical analogues already cuts down the endless array of possibilities to an arbitrary set of crystals. The total set of crystals, with distinction between the calculated and not calculated crystals, is visualised in the ternary phase diagram in figure 5.1. Some data points have multiple possible space groups. The crystals for which the formation energy could be determined are listed in table 5.1.

Original crystal	Space group	cif-nr.	New crystal
$\text{Sn}_5\text{Sb}_2\text{S}_9$	Pbca	200500	$\text{Pb}_5\text{Bi}_2\text{Po}_9/\text{Pb}_5\text{Bi}_2\text{Te}_9$
GeAsSe	Pnna	100828	PbBiPo/PbBiTe
$\text{Pb}_6\text{Bi}_2\text{S}_9$	Cmcm	186916	$\text{Pb}_6\text{Bi}_2\text{Po}_9/\text{Pb}_6\text{Bi}_2\text{Te}_9$
$\text{Pb}_2\text{Bi}_2\text{S}_5$	Pbnm	43657	$\text{Pb}_2\text{Bi}_2\text{Po}_5/\text{Pb}_2\text{Bi}_2\text{Te}_5$
$\text{Sn}_2\text{Sb}_2\text{S}_5$	Pnma	650823	$\text{Pb}_2\text{Bi}_2\text{Po}_5/\text{Pb}_2\text{Bi}_2\text{Te}_5$
$\text{Pb}_2\text{Bi}_2\text{Te}_5$	$\text{P}\bar{3}\text{m1}$	100295	$\text{Pb}_2\text{Bi}_2\text{Po}_5/\text{Pb}_2\text{Bi}_2\text{Te}_5$

$\text{Sn}_2\text{P}_2\text{S}_6$	$\text{R}\bar{3}\text{H}$	648055	$\text{Pb}_2\text{Bi}_2\text{Po}_6/\text{Pb}_2\text{Bi}_2\text{Te}_6$
$\text{Sn}_2\text{P}_2\text{Se}_6$	$\text{P}121/\text{c}1$	648114	$\text{Pb}_2\text{Bi}_2\text{Po}_6/\text{Pb}_2\text{Bi}_2\text{Te}_6$
$\text{Pb}_3\text{Bi}_2\text{S}_6$	$\text{C}12/\text{m}1$	92981	$\text{Pb}_3\text{Bi}_2\text{Po}_6/\text{Pb}_3\text{Bi}_2\text{Te}_6$
$\text{Ge}_3\text{As}_2\text{Te}_6$	$\text{R}\bar{3}\text{mH}$	68113	$\text{Pb}_3\text{Bi}_2\text{Po}_6/\text{Pb}_3\text{Bi}_2\text{Te}_6$
SnBi_4Te_7	$\text{P}\bar{3}\text{m}1$	236253	$\text{PbBi}_4\text{Po}_7/\text{PbBi}_4\text{Te}_7$
$\text{Pb}_4\text{Sb}_4\text{S}_{11}$	Pbam	200601	$\text{Pb}_4\text{Bi}_4\text{Po}_{11}/\text{Pb}_4\text{Bi}_4\text{Te}_{11}$
$\text{Ge}_4\text{As}_2\text{Te}_7$	$\text{R}\bar{3}\text{mH}$	68114	$\text{Pb}_4\text{Bi}_2\text{Po}_7/\text{Pb}_4\text{Bi}_2\text{Te}_7$
$\text{PbBi}_6\text{Te}_{10}$	$\text{R}\bar{3}\text{mH}$	95551	$\text{PbBi}_6\text{Po}_{10}/\text{PbBi}_6\text{Te}_{10}$
PbBi_2S_4	Pnma	616916	$\text{PbBi}_2\text{Po}_4/\text{PbBi}_2\text{Te}_4$
GeBi_2Te_4	$\text{R}\bar{3}\text{mH}$	658633	$\text{PbBi}_2\text{Po}_4/\text{PbBi}_2\text{Te}_4$
PbSb_2Te_4	$\text{P}\bar{3}\text{m}1$ ¹	250250	$\text{PbBi}_2\text{Po}_4/\text{PbBi}_2\text{Te}_4$
SnPS_3	$\text{P}121/\text{c}1$	657344	$\text{PbBiPo}_3/\text{PbBiTe}_3$
$\text{Pb}_3\text{Sb}_8\text{S}_{15}$	$\text{C}12/\text{c}1$	94852	$\text{Pb}_3\text{Bi}_8\text{Po}_{15}/\text{Pb}_3\text{Bi}_8\text{Te}_{15}$

TABLE 5.1: From left to right: (1) Original experimental crystals, (2) corresponding space group, (3) index number of the CIF-file in ICSD, (4) crystal with substituted Bi- and Po/Te-atoms.

5.2 Stability of the ternary crystals

The formation energies of all ternary crystals that are calculated are shown in table B.1. Columns three and four display the formation energies with respect to the elementary solids. Although these energies do not contain any physical information about the stability, they will be of interest when one wants to determine a correlation between the Po- and Te-containing crystals. Almost all crystals, with Po or Te, have a negative formation energy when compared to the elementary solids. The Te-containing crystals have a systematically lower (more negative or less positive) energy than the crystals containing Po, which is in accordance with the results of the binary phases.

The physically relevant formation energies, i.e. the formation energies with respect to the decomposition in these most stable binary and elementary crystals, are summarized in the fifth and sixth column of table B.1. If one visualizes these crystals in a ternary phase diagram (see figure 5.2), and one adds the binary phase diagrams calculated in chapter 4 one can see that a lot of these crystals can be decomposed as the two stable binary phases PbPo/Te and $\text{Bi}_2(\text{Po/Te})_3$. Another trend is visible: there are four crystals on the path connecting elementary Po/Te with PbBi . In section 4.2 it was argued that there are no stable phases for PbBi . Decomposition hence exist of a combination of elementary Po/Te, PbPo/Te and $\text{Bi}_2(\text{Po/Te})_3$.

¹Space group selected by WIEN2k. The original space group mentioned in ICSD was $\text{R}\bar{3}\text{H}$.

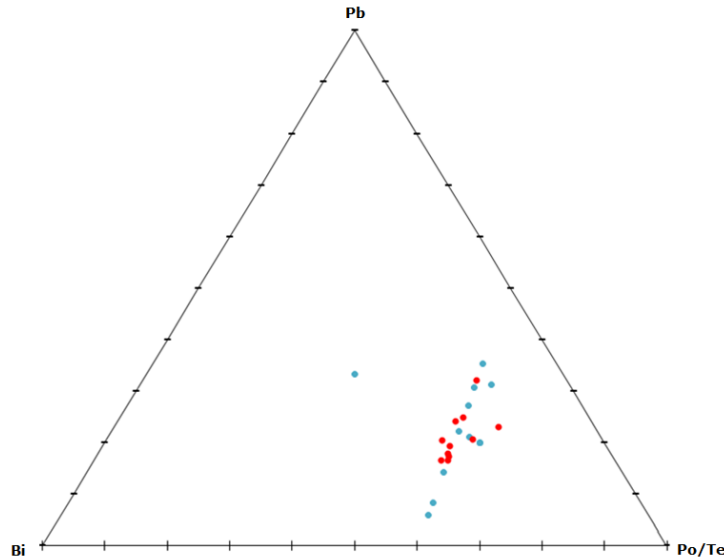


FIGURE 5.1: Set of ternary crystals origination from the third to the sixth period of the PSE. Blue data points are calculated. Red data points could not be calculated due to computational limitations (see text).

One finds only one marginally stable Po- and one marginally stable Te-crystal when looking at the real formation energies. The energy is in both cases so small (an order of magnitude below the accuracy of the calculations) that it is uncertain that these structures are indeed stable. Furthermore, one can observe that the Te-based crystals are no longer systematically more stable than the Po-crystals, as was the case for the binary phases. This can be explained by the greater stability of binary Te-crystals when compared to their Po-containing counterparts. The ternary Te-crystals have a consistently lower (more negative or less positive) formation energy when decomposition in elementary solids is imposed. The more stable binary Te-crystals will counteract this effect, leading to Po- and Te- crystals with similar stability. A more quantitative relation is deduced in section 5.3.

The positive formation energies in (nearly) all cases show that decomposition of the ternary phases into Bi_2X_3 and PbX is favourable. The cross section of the Pb-Bi-Po and Pb-Bi-Te phase diagrams, indicated in figure 5.2, can be visualised in a two-dimensional way, which is done in figure 5.3. All formation energies of the crystals in figure 5.3 lie above the convex hull (or are marginally stable in two cases), the values lie in all cases less than 0,1 eV/atom above the convex hull. Considering to the earlier mentioned example of the metastable ZnO_2 (figure 1.3) lying 0,1 eV/atom above the convex hull, none of these crystals can be declared unstable with certainty.

In order to investigate the reliability of the results in table B.1, a comparison can be made with the data of Materials Project [1], where three ternary Pb-Bi-Te-phases were calculated. These results, calculated with VASP, are compared to the WIEN2k-results from this thesis in table 5.2. If one compares the formation energy with respect to the elementary solids, one can see an

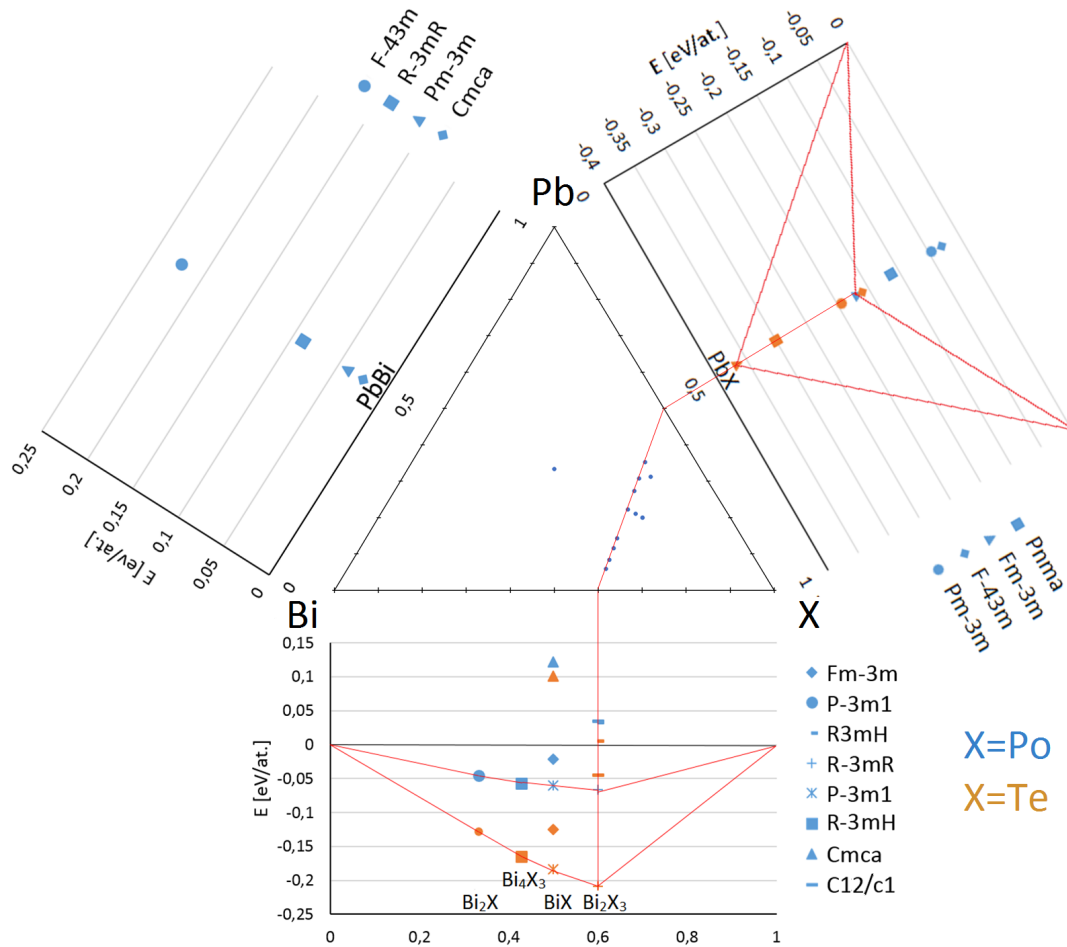


FIGURE 5.2: Decomposition of the ternary crystals into stable binary phases. Blue data points correspond to $X=Po$. Orange data points correspond to $X=Te$.

overestimation of the energy by VASP ranging from 0,032 eV/atom to 0,036 eV/atom. A similar overestimation of the energy was found for the binary crystals in table 4.4. The WIEN2k- and VASP-calculations agree that the three ternary crystals of table 5.2 are unstable/metastable. The formation energy calculated by WIEN2k and VASP corresponds really well for $PbBi_4Te_7$ and $PbBi_2Te_4$, with an energy difference of only 0,002 eV/atom. The difference in formation energy of $Pb_2Bi_2Te_5$ for both DFT codes is slightly larger: 0,034 eV/atom.

$Pb_2Bi_2Te_5$ has a formation energy above the convex hull. However, in Ref. [48], Silkin et al. show from first principles that $Pb_2Bi_2Te_5$ is a three-dimensional topological insulator. In the article, no information about the (meta)stability of this material is given however. This crystal lies 0,017 eV/atom above the convex hull according to the WIEN2k- and the VASP-calculations. As was mentioned in chapter 4, ZnO_2 , lying 0,1 eV/atom above the convex hull is still metastable

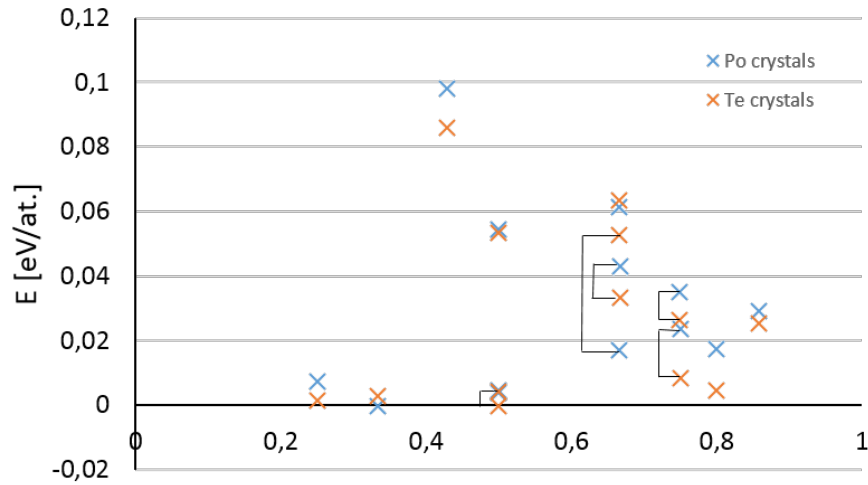


FIGURE 5.3: Formation energy of the crystals that are composed of Bi_2Po_3 and PbPo . Corresponding crystal structures for Po- and Te-crystals are represented by the same symbol. From left to right (and from less to more stable for the Te-crystals in case of multiple structures): $\text{PbBi}_6\text{X}_{10}$, PbBi_4X_7 , $\text{Pb}_3\text{Bi}_8\text{X}_{15}$, PbBi_2X_4 (Pnma), PbBi_2X_4 ($\text{R}\bar{3}\text{mH}$), PbBi_2X_4 ($\text{P}\bar{3}\text{m1}$), $\text{Pb}_2\text{Bi}_2\text{X}_5$ (Pnma), $\text{Pb}_2\text{Bi}_2\text{X}_5$ ($\text{P}\bar{3}\text{m1}$), $\text{Pb}_2\text{Bi}_2\text{X}_5$ (Pbnm), $\text{Pb}_3\text{Bi}_2\text{X}_6$ ($\text{C}2/\text{m}$), $\text{Pb}_3\text{Bi}_2\text{X}_6$ ($\text{R}\bar{3}\text{mH}$) $\text{Pb}_4\text{Bi}_2\text{X}_7$ and $\text{Pb}_2\text{Bi}_6\text{X}_9$.

[2]. The conclusion that $\text{Pb}_2\text{Bi}_2\text{Te}_5$ ($\text{P}\bar{3}\text{m1}$) could be metastable is acceptable.

Formula	Space Group	WIEN2k (El.) [eV/at.]	VASP (El.) [eV/at.]	ΔE [eV/at.]	WIEN2k (ΔE) [eV/at.]	VASP (ΔE) [eV/at.]	ΔE [eV/at.]
PbBi_4Te_7	P-3m1	-0,232	-0,266	0,034	0,003	0,001	-0,002
PbBi_2Te_4	R-3m	-0,250	-0,286	0,036	0,005	0,001	-0,002
$\text{Pb}_2\text{Bi}_2\text{Te}_5$	P-3m1	-0,226	-0,258	0,032	0,052	0,186	-0,034

TABLE 5.2: Comparison of data points of the Pb-Bi-Te phase diagram, calculated by WIEN2K and VASP. Columns from left to right: (1) Chemical formula of the crystal, (2) corresponding space group, the formation energy energy in comparison with the elementary solids, calculated with WIEN2k (3) and VASP (4), (5) the energy difference between the WIEN2k- and the VASP-result, the formation energy (in comparison with the decomposition in stable binary crystals) calculated by WIEN2k (6) and VASP (7) and (8) the energy difference between the WIEN2k- and the VASP-result.

5.3 Correlation between ternary phases containing Po and Te

The correlation diagram in figure 4.8 that was determined in chapter 4 can now be expanded by adding the ternary crystals. For the results to be comparable, the formation energies of the ternary phases have to be determined with respect to the elementary solids. The results are visualised in figure 5.4. A correlation is visible and after a least-squares fit, the following equation can be formulated:

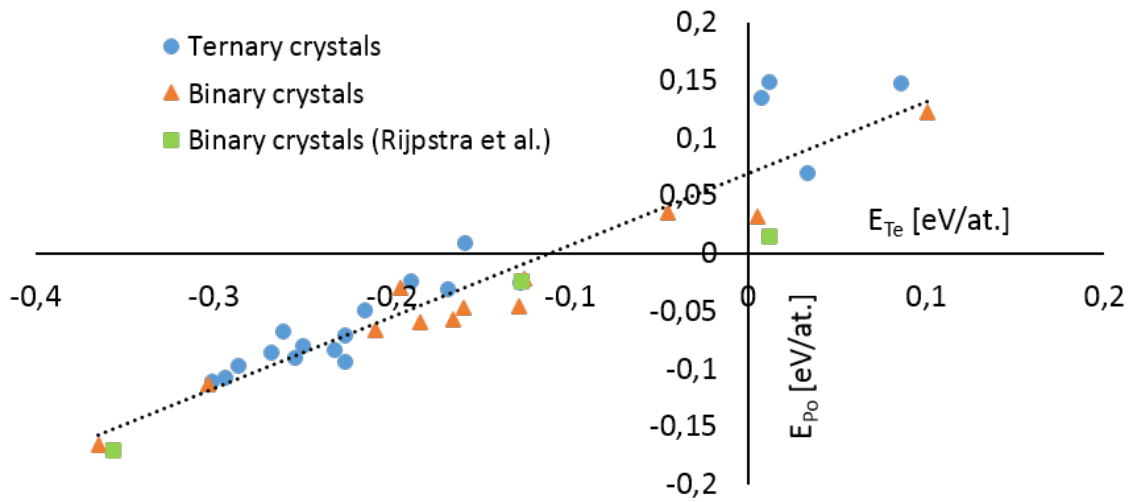
$$\Delta E_{Po}[eV/at.] = 0,621 \cdot \Delta E_{Te}[eV/at.] + 0,069eV/at. \quad (5.1)$$

The determination coefficient R^2 of this correlation equals 0,89. The addition of more data leads to a similar equation as correlation 4.4, which is visually verifiable by comparing the data points of the binary and ternary crystals in figure 5.4. When one correlates the formation energy of Po and Te with respect to the most stable decomposition (no longer limited to elementary solids, i.e. the actual formation energy), one finds the graph displayed in figure 5.5. A correlation is still present and can be written as:

$$\Delta E_{Po}[eV/at.] = 0,770 \cdot \Delta E_{Po}[eV/at.] + 0,009eV/at. \quad (5.2)$$

The determination coefficient of this correlation equals 0,94. Correlations 5.1 and 5.2 cannot be compared due to the different definition of formation energy. A consequence of figure 5.4 is that the correlation between formation energies with respect to elementary solids for Te-based and Po-based compounds are correlated, irrespective of the complexity of the crystal (binary, ternary, and most likely beyond ternary as well). A similar strategy as demonstrated in section 4.5 to convert formation energies for Te-based compounds into equivalent values for Po-based compounds (which are much harder to measure experimentally) can therefore be applied. The scatter around the linear fit in figure 5.4 suggests that the conversion is more reliable for Te-compounds that are more strongly bound with respect to the elementary crystals (-0,2 eV/atom and below).

The DFT predictions of the formation energies of the Bi_2Po_3 - PbPo cross section of the ternary Pb-Bi-Po phase diagram can be compared with the formation energies one can deduce by using formula 5.2. The result is visualized in figure 5.6. The matching data points compare well, indicating that reliable predictions of the Pb-Bi-Po system can be made by experimental research of the Pb-Bi-Te system.



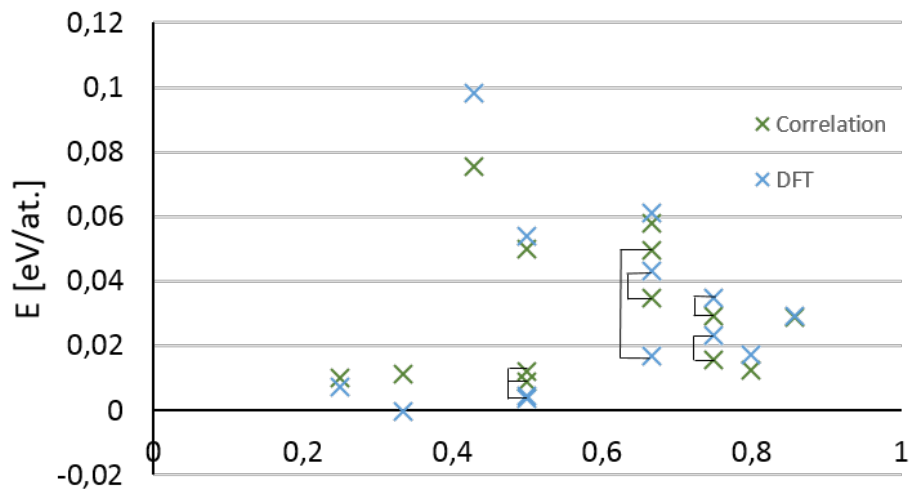


FIGURE 5.6: Comparison between the DFT formation energies and the formation energies obtained using the correlation with the Pb-Bi-Te phase diagram for the Bi₂Po₃ - PbPo cross section of the ternary Pb-Bi-Pophase diagram. Corresponding crystal structures for Po- and Te-crystals are represented by the same symbol. From left to right (and from less to more stable for the Te-crystals in case of multiple structures): PbBi₆X₁₀, PbBi₄X₇, Pb₃Bi₈X₁₅, PbBi₂X₄ (Pnma), PbBi₂X₄ (R $\bar{3}$ mH), PbBi₂X₄ (P $\bar{3}$ m1), Pb₂Bi₂X₅ (Pnma), Pb₂Bi₂X₅ (P $\bar{3}$ m1), Pb₂Bi₂X₅ (Pbnm), Pb₃Bi₂X₆ (C2/m), Pb₃Bi₂X₆ (R $\bar{3}$ mH) Pb₄Bi₂X₇ and Pb₂Bi₆X₉.

Chapter 6

Conclusion and Outlook

In this thesis the ternary Pb-Bi-Po and Pb-Bi-Te phase diagrams were determined by DFT. The selected search space of possible stable candidate structures was based on chemical similarity with experimentally observed crystals made from elements of the same groups. All experimental crystallographic information was extracted from ICSD. The advantage of database searching shows itself in the high possibility of finding stable structures using a relatively small data set. A disadvantage is the inability to predict stable crystals that do not have an experimentally known analogue.

First, the binary sections of the ternary phase diagrams of Pb-Bi-Po and Pb-Bi-Te were investigated. DFT calculations for Te-crystals compared well to experimental data (every phase that DFT predicts to be stable is indeed observed experimentally) and to VASP-calculations, taken from Materials Project. The convincing correspondence between the formation energies (calculated from first principles) of binary Te-crystals is a promising sign that all predictions of stable binary Po-phases (which are the same as for the binary Te-phases), and in extension the predictions for the ternary Pb-Bi-Po and Pb-Bi-Te crystals, are reliable. Hence, the existence of four new binary Bi-Po crystals that are not yet known experimentally is predicted.

Thereafter, the ternary phases were examined. Neither for Pb-Bi-Po nor for Pb-Bi-Te a ternary crystal was found that was significantly stable against decomposition in binary or elementary crystals. It therefore takes energy to create such crystals at 0 K. However, several of these positive formation energies are rather small ($< 0,1$ eV/atom, a few even $< 0,01$ eV/atom). This makes it easily possible that these ternary crystals can exist at room temperature. They could be either stable crystals if entropy contributions would make the decomposition into binary and elementary crystals unfavourable at elevated temperature, or they could be metastable crystals if an energy barrier prevents their spontaneous decomposition. As a message to experimental phase diagram research, we therefore explicitly suggest to consider the room temperature stability of PbBi_4X_7 , PbBi_2X_4 , $\text{PbBi}_6\text{X}_{10}$, $\text{Pb}_2\text{Bi}_2\text{X}_5$, $\text{Pb}_2\text{Bi}_4\text{X}_7$, $\text{Pb}_2\text{Bi}_3\text{X}_6$, $\text{Pb}_2\text{Bi}_6\text{X}_9$, $\text{Pb}_3\text{Bi}_2\text{X}_6$ and $\text{Pb}_3\text{Bi}_8\text{X}_{15}$ (ordered according to decreasing likelihood to exist).

There are a few obvious computational ways to increase the knowledge about these phase diagrams further. They are listed here according to increasing computational cost. (1) By performing phonon calculations for all considered phases, the temperature dependent free energy could be determined and (meta)stability at a given temperature can be predicted. (2) Unbiased crystal structure prediction methods (see section 1.1.2.3) can be applied to find possibly more stable crystal structures of the stoichiometries that were considered in this work, and to obtain the most favourable crystal structure for other stoichiometries for which no chemical analogues do exist. (3) Methods from transition state theory can be used to assess the height of the energy barriers, which would indicate which metastable crystals are more likely to survive.

Besides the stability of the ternary phases, a relation between Po- and Te-containing crystals was proven. This correlation is of importance for experimental scientists. In certain experiments Po can be replaced by the safer Te, after which the correlation between both elements that was determined in this work can be invoked to convert the experimental information for Te variants into information for the corresponding Po variants.

Appendix A

Binary Phase Results

Formula	Space group	CIF-nr.	E [eV/at.]
PbBi	Pm $\bar{3}$ m	651575	0,0408
PbBi	F $\bar{4}$ 3m	53968	0,2231
PbBi	R $\bar{3}$ mR	52294	0,0892
PbBi	Cmca	160382	0,0229
PbPo	Pnma	648582	-0,1131
PbPo	Fm $\bar{3}$ m	105598	-0,1666
PbPo	F $\bar{4}$ 3m	53956	-0,0300
PbPo	Pm $\bar{3}$ m	604129	-0,0474
BiPo	Fm $\bar{3}$ m	44984	-0,0219
BiPo	P $\bar{3}$ m1	617181	-0,0602
BiPo	Cmca	160382	0,1217
Bi ₂ Po	P $\bar{3}$ m1	69557	-0,0456
Bi ₄ Po ₃	R $\bar{3}$ mH	30526	-0,0571
Bi ₂ Po ₃	R3mH	20289	0,0322
Bi ₂ Po ₃	R $\bar{3}$ mR	15753	-0,0665
Bi ₂ Po ₃	C12/c1	185954	0,0352
PbTe	Pnma	648582	-0,3027
PbTe	Fm $\bar{3}$ m	105598	-0,3643
PbTe	F $\bar{4}$ 3m	53956	-0,1950
PbTe	Pm $\bar{3}$ m	604129	-0,1594
BiTe	Fm $\bar{3}$ m	44984	-0,1256
BiTe	P $\bar{3}$ m1	617181	-0,1842
BiTe	Cmca	160382	0,1011
Bi ₂ Te	P $\bar{3}$ m1	69557	-0,1284
Bi ₄ Te ₃	R $\bar{3}$ mH	30526	-0,1651
Bi ₂ Te ₃	R3mH	20289	0,0053
Bi ₂ Te ₃	R $\bar{3}$ mR	15753	-0,2093
Bi ₂ Te ₃	C12/c1	185954	-0,0452

TABLE A.1: Columns from left to right: (1) all investigated binary phases of the Pb-Bi-Po and Pb-Bi-Te systems, (2) corresponding space group,(3) index of the CIF in ICSD, (4) formation energy in ev/atom.

Appendix B

Ternary Phase Results

Formula	Space Group	$E_{X=Po}$ w.r.t. el. [eV/at.]	$E_{X=Te}$ w.r.t. el. [eV/at.]	$E_{X=Po}$ [eV/at.]	$E_{X=Te}$ [eV/at.]
Pb ₅ Bi ₂ X ₉	Pbca	-0,0245	-0,1888	0,1004	0,1043
PbBiX	Pnna	0,1467	0,0860	0,2581	0,3289
Pb ₆ Bi ₂ X ₉	Cmcm	-0,1080	-0,2933	0,0291	0,0254
Pb ₂ Bi ₂ X ₅	Pbnm	-0,0679	-0,2607	0,0430	0,0333
Pb ₂ Bi ₂ X ₅	Pnma	-0,0498	-0,2151	0,0612	0,0631
Pb ₂ Bi ₂ X ₅	P $\bar{3}$ m1	-0,0941	-0,2258	0,0169	0,0524
Pb ₂ Bi ₂ X ₆	R $\bar{3}$ H	0,0689	0,0333	0,1687	0,2837
Pb ₂ Bi ₂ X ₆	P121/c1	0,1350	0,0072	0,2349	0,2576
Pb ₃ Bi ₂ X ₆	C12/m1	-0,0864	-0,2677	0,0346	0,0262
Pb ₃ Bi ₂ X ₆	R $\bar{3}$ mH	-0,0976	-0,2856	0,0234	0,0083
PbBi ₄ X ₇	P $\bar{3}$ m1	-0,0835	-0,2322	-0,0004	0,0029
Pb ₄ Bi ₄ X ₁₁	Pbam	-0,0309	-0,1687	0,0742	0,0949
Pb ₄ Bi ₂ X ₇	R $\bar{3}$ mH	-0,1109	-0,3005	0,0172	0,0042
PbBi ₆ X ₁₀	R $\bar{3}$ mH	-0,0708	-0,2263	0,0074	0,0013
PbBi ₂ X ₄	Pnma	-0,0261	-0,1276	0,0541	0,0531
PbBi ₂ X ₄	R $\bar{3}$ mH	-0,0801	-0,2498	0,0035	0,0038
PbBi ₂ X ₄	P $\bar{3}$ m1	-0,0907	-0,2541	0,0044	-0,0005
PbBiX ₃	P121/c1	0,1485	0,0120	0,2484	0,2624
Pb ₃ Bi ₈ X ₁₅	C12/c1	0,0085	-0,1591	0,0981	0,0859

TABLE B.1: Columns from left to right: (1) all investigated ternary crystals (with X=Po or Te), (2) the corresponding space group, (3) the formation energy w.r.t. the elementary solids of the Po-crystals (3) and the Te-crystals (4), the formation energy w.r.t. decomposition in stable binary and/or elementary crystals of the Po-crystals (5) and of the Te-crystals (6).

Bibliography

- [1] <https://www.materialsproject.org>
- [2] K. Rijpstra. Density functional theory as a tool to get more out of experimental data: case-studies for Al-Zn-O and for the interaction between Po and Pb-Bi-eutectic. 2014.
- [3] S. Hao, L. Zhao, C. Chen, V. P. Dravid, M. G. Kanatzidis and C. M. Wolverton. Theoretical Prediction and Experimental Confirmation of Unusual Ternary Ordered Semiconductor Compounds in Sr-Pb-S System. *J. Am. Chem. Soc.*, 136 (4), pp 1628–1635. 2014.
- [4] A. van de Walle, Z. Moser and W. Gasior. First-Principles Calculation of the Cu-Li Phase Diagram. *Archives of Metallurgy and Materials*, 49 (3). pp. 535-544. 2004.
- [5] D. De Fontaine, A. G. Evans, J. P. Hirth, P. M. Levy, R. C. Pond, F. Spaepen and F. W. Zok. Solid State Physics vol.47. *Academic Press*. 1994.
- [6] J. Teeriniemi, P. Taskinen and K. Laasonen. First-principles investigation of the Cu-Ni, Cu-Pd, and Ni-Pd binary alloy systems. *Intermetallics*, 57(0), 41–50. 2015.
- [7] A. Seko, Y. Koyama and I. Tanaka. Cluster expansion method for multicomponent systems based on optimal selection of structures for density-functional theory calculations. *Physical Review B* 80:165122. 2009.
- [8] A. van de Walle, M. Asta and G. Ceder. The alloy theoretic automated toolkit: A user guide. *Calphad*, 26(4), 539-553. 2002.
- [9] J. M. Sanchez . Cluster expansion and the configurational theory of alloys. *Phys. Rev. B* 81:224202. 2010.
- [10] C. J. Pickard and R. J. Needs. Ab initio Random Structure Searching. *J. Phys.: Condens. Matter* 23(5):053201. 2011.
- [11] W. W. Tipton and R. G. Hennig. A grand canonical genetic algorithm for the prediction of multi-component phase diagrams and testing of empirical potentials. *J. Phys.: Condens. Matter*, 25(49):495401. 2013.
- [12] <http://myrrha.sckcen.be>
- [13] B. Povh, K. Rith, C. Scholz and F. Zetsche. Particles and Nuclei, An Introduction to the Physical Concepts, 6th ed. *Springer*. 2006.

- [14] H. A. Abderrahim, P. Baeten, D. De Bruyn and R. Fernandez. MYRRHA - A multi-purpose fast spectrum research reactor. *Energy Conversion and Management*, 63(0):4–10. 2012.
- [15] H. A. Abderrahim, P. Kupschus, E. Malambu, P. Benoit, K. Van Tichelen, B. Arien, F. Vermeersch, P. Dhondt, Y. Jongen, S. Ternier and D. Vandeplassche. MYRRHA: A multi-purpose accelerator driven system for research and development. *Nuclear Instruments and Methods in Physics Research Section A: Accelerators, Spectrometers, Detectors and Associated Equipment*, 463(3):487–494. 2001.
- [16] K. Van Tichelen, B. Arien, F. Vermeersch, Y. Jongen, S. Ternier, and D. Vandeplassche. MYRRHA: a multipurpose accelerator driven system for research and development. *Power reactors and sub-critical blanket systems with lead and lead-bismuth as coolant and/or target material* p.163. 2003.
- [17] C. Fazio *Handbook on Lead-bismuth Eutectic Alloy and Lead Properties, Materials Compatibility, Thermal-hydraulics and Technologies*. OECD/NEA. 2007.
- [18] K. Rijpstra, A. Van Yperen-De Deyne, J. Neuhausen, V. Van Speybroeck and S. Cottenier. Solution enthalpy of Po and Te in solid lead-bismuth eutectic. *Journal of Nuclear Materials*, 450(1-3):287–291. 2014.
- [19] H. Feuerstein, J. Oschinski and S. Horn. Behavior of Po-210 in Molten Pb-17Li. *Journal of Nuclear Materials*, 191-194, Part A(0):288-291. 1992.
- [20] L.O. Amaya and J. Braet. Purification of Lead-Bismut Eutectic Used in Accelerator Driven Systems. *WM2009 Conference*. 2009.
- [21] J. Buongiorno, E.P. Loewen, K. Czerwinski and C. Larson. Studies of Polonium Removal from Molten Lead-Bismuth for Lead-Alloy-Cooled Reactor Applications. *Nuclear Technology*, 147 406-417. 2004.
- [22] E.P. Loewen and L.E. Auman. Investigation of polonium removal systems for lead-bismuth cooled FBRs. *Progress in Nuclear Energy*, 47(1-4):586-595. 2005.
- [23] W. Kohn and L. J. Sham. Self-consistent equations including exchange and correlation effects. *Phys. Rev.*, 140:A1133–A1138. 1965.
- [24] P. Hohenberg and W. Kohn. Inhomogeneous Electron Gas. *Phys. Rev.* 136:B864-B871. 1964.
- [25] S. Cottenier, *Density Functional Theory and the family of (L)APW-methods: a step-by-step introduction*, 2002-2013 (2nd edition), ISBN 978-90-807215-1-7 (freely available at http://www.wien2k.at/reg_user/textbooks).
- [26] J. M. Ziman. Principles of the Theory of Solids, 2nd ed. *Cambridge University Press*, chapt. 6, 200-203. 1972.
- [27] J. P. Perdew, K. Burke, and M. Ernzerhof. Generalized gradient approximation made simple. *Phys. Rev. Lett.*, 77:3865-3868. 1996.

- [28] J. P. Perdew, J. A. Chevary, S. H. Vosko; K. A. Jackson; M. R. Pederson, D. J. Singh and C. Fiolhais. Atoms, molecules, solids, and surfaces: Applications of the generalized gradient approximation for exchange and correlation. *Phys. Rev. B*, 46:6671-6687. 1992.
- [29] A. D. Becke. Density-functional exchange-energy approximation with correct asymptotic behavior. *Phys. Rev. A* 38:3098-3100. 1988.
- [30] D. C. Langreth and M. J. Mehl. Beyond the local-density approximation in calculations of ground-state electronic properties. *Phys. Rev. B* 28: 1809-1834. 1983.
- [31] P. Blaha, K. Schwarz, P. Sorantin and S. B. Trickey. Full-potential, linearized augmented plane wave programs for crystalline systems. *Computer Physics Communications*, 59(2):399-415. 1990.
- [32] E. Sjöstedt, L. Nordström and D. J. Sing. An alternative way of linearizing the augmented plane-wave method. *Solid State Commun.*, 114(1):15-20. 2000.
- [33] P. A. M. Dirac. The Quantum Theory of the Electron. *Proceedings of the Royal Society Series A, Containing Papers of a Mathematical and Physical Character*, 117(778):610-624. 1928.
- [34] B.H. Bransden and C.J. Joachain. Physics of atoms and molecules 2nd ed. *Prentice Hall*. 2003.
- [35] P. Novak. LDA+U, energy and potential, why there is spin nondiagonal part and what is its for. 2003.
- [36] P. Novak. Calculation of spin-orbit coupling.
- [37] X. Rocquefelte. Relativistic effects and Non-collinear magnetism (WIEN2k / WIENncm). 20th WIEN2k Workshop PennStateUniversity. 2013.
- [38] C. Kittel. Introduction to Solid State Physics. *John Wiley and Sons, inc.*, 1996.
- [39] P. Novak. Lecture on spinorbit. 1997.
- [40] D. Singh. Plane waves, pseudopotentials and the LAPW method. *Springer*. 1994.
- [41] K. Refson. Practical calculations using first-principles QM. Convergence, convergence, convergence. 2007.
- [42] Birch, F. Finite elastic strain of cubic crystals. *Phys. Rev.*, 71:809–824. 1947.
- [43] L. D. Marks. ReadMe file for new version of mixer (VER5.3). 2012.
- [44] <http://www.r-project.org>
- [45] Alloy Phase Diagrams Volume 3. *ASM International*. 1992.
- [46] <http://www.crystallography.net>

-
- [47] K. Lejaeghere, V. Van Speybroeck, G. Van Oost and S. Cottenier. Error estimates for solid-state density-functional theory predictions: an overview by means of the ground-state elemental crystals. *Critical reviews in solid state and materials sciences*, 39(1):1–24. 2014.
- [48] I. V. Silkin, Yu. M. Koroteev, S. V. Eremeev, G. Bihlmayer and E. V. Chulkov, Three and Two-dimensional Topological Insulators in $\text{Pb}_2\text{Sb}_2\text{Te}_5$, $\text{Pb}_2\text{Bi}_2\text{Te}_5$, and $\text{Pb}_2\text{Bi}_2\text{Se}_5$ Layered Compounds. *JETP Letters*, 94(3):217-221. 2011.